PAPER • OPEN ACCESS

Interphase formation with carboxylic acids as slurry additives for Si electrodes in Li-ion batteries. Part 2: a photoelectron spectroscopy study

View the article online for updates and enhancements.

Journal of Physics: Energy

Interphase formation with carboxylic acids as slurry additives for Si electrodes in Li-ion batteries. Part 2: a photoelectron spectroscopy study

Fabian Jeschull[1,2,*] ⓘ, Hieu Quang Pham[1,4] ⓘ, Ahmad Ghamlouche[2] ⓘ, Pardeep K Thakur[3] ⓘ, Sigita Trabesinger[1,*] ⓘ and Julia Maibach[2] ⓘ

[1] Battery Electrodes and Cells, Electrochemistry Laboratory, Paul Scherrer Institute (PSI), Forschungsstrasse 111, Villigen PSI, 5232, Switzerland
[2] Institute for Applied Materials—Energy Storage Systems (IAM-ESS), Karlsruhe Institute of Technology, Hermann-von-Helmholtz-Platz 1, 76344 Eggenstein-Leopoldshafen, Germany
[3] Diamond Light Source Ltd, Diamond House, Harwell Science and Innovation Campus, Didcot, Oxfordshire OX11 0DE, United Kingdom
[4] Current affiliation: InoBat Auto, Mostová 6, 811 02 Bratislava, Slovakia.
* Authors to whom any correspondence should be addressed.

E-mail: fabian.jeschull@kit.edu and sigita.trabesinger@psi.ch

Abstract

Preparing aqueous silicon slurries in presence of a low-pH buffer improves the cycle life of silicon electrodes considerably because of higher reversibility of the alloying process and higher resilience towards volume changes during (de)alloying. While the positive effects of processing at low pH have been demonstrated repeatedly, there are gaps in understanding of the buffer's role during the slurry preparation and the effect of buffer residues within the electrode during cycling. This study uses a combination of soft and hard x-ray photoelectron spectroscopy to investigate the silicon particle interface after aqueous processing in both pH-neutral and citrate-buffered environments. Further, silicon electrodes are investigated after ten cycles in half-cells to identify the processing-dependant differences in the surface layer composition. By tuning the excitation energy between 100 eV and 7080 eV, a wide range of probing depths were sampled to vertically map the electrode surface from top to bulk. The results demonstrate that the citrate-buffer becomes an integral part of the surface layer on Si particles and is, together with the electrode binder, part of an artificial solid-electrolyte interphase that is created during the electrode preparation and drying.

1. Introduction

Silicon as active material for negative electrodes in Li-ion batteries is of high interest owing to its high Li-storage capability, reaching up to 3579 mAh g^{-1} (Li$_{15}$Si$_4$) in the fully lithiated state at room temperature [1]. This would correspond to nearly a ten-fold increase in specific capacity in comparison to the commonly used graphite negative electrode. However, this tremendous enhancement in capacity comes with a penalty: the Si particles expand by about 300% upon lithiation [2]. As a result, particle rearrangements caused by the expanding and contracting individual particles lead to notable changes in the particle wiring during cycling that can ultimately result in intermittent or total isolation of Si subdomains [3] in the electrode, as well as loss of contact to the current collector. On top of these issues, the passivation layer formed by electrolyte decomposition reactions, known as the solid-electrolyte interphase (SEI), is inherently unstable due to the recurrent volume changes of the Si particles [4, 5]. As the SEI breaks repeatedly, unprotected Si surface is exposed and new decomposition reactions are initiated, contributing to a growth of the SEI layer and thus to increasing internal resistances [4], pore clogging [6] and particle isolation. The formation of HF from electrolyte salt degradation (e.g. with trace amounts of water) is a particular problem as it leads to etching of

the native silicon oxide layer on the active material particles that induce further changes of the electrode–electrolyte interface [4, 7, 8].

One proven approach to mitigate the effects of volume change and improve the interfacial properties of the electrode material is to use water-soluble binders, such as polysaccharides (e.g. carboxymethyl cellulose sodium salt, CMC–Na) [9–11], polyacrylic acid (PAA–H) or its salts (PAA–X; X = Li, Na, K, Mg, etc) [12, 13]. These established binders show higher resilience towards the mechanical stress upon volume changes, as compared to poly(vinylidene difluoride)-based binders [14–16]. Depending on their amount, flocculation, and networking behaviour, binders control the particle dispersion in the slurry and thus their distribution in the final electrode coating [9, 17, 18]. As such, binders act as surfactants at the particle interface and remain there after casting and drying of the slurry. Previous results suggest that binders such as CMC–Na are participating in the SEI formation process during the first cycles. On the one hand, they have functional groups, i.e. carbonyl groups, that are susceptible to reduction reactions and are thus likely to decompose to a certain degree at low potentials [19, 20]. On the other hand, results indicate that the polymers influence the deposition and growth of electrolyte decomposition products, leading to altered SEI layer properties, e.g. thinner layers, smaller grain sizes of inorganic components and a more even distribution on the particle surface [21, 22]. As a polymer layer, binders are located directly on the particle surface and may reduce direct exposure of electrode components to electrolyte [13, 23–25], acting as an 'artificial' SEI layer. These benefits are reflected in higher Coulombic efficiencies and slower capacity fade as compared to the conventional fluorinated binders [18].

Lestriez *et al* further enhanced the beneficial properties of the binder by preparing slurries in a citric-acid buffered environment at low pH [26–28]. The resulting Si electrodes show smaller volume expansion of the electrode during cycling, indicating a higher resilience towards the detrimental effects, induced by the alloying reaction between lithium and silicon [29]. Other studies propose that cross-linking reactions, occurring between the carboxylic-acid and the binder, form an interconnected polymer network that might withstand the electrode breathing process better [30]. Chemically, carboxylic acids and CMC–Na or PAA–H have the same functional groups, only that carboxylic acids lack the polymeric backbone. In fact, citric acid and CMC–Na show similar features in infrared (IR) spectra [31], suggesting that similar surface processes (i.e. surface adsorption [31–33] or covalent bonding [14, 26, 34, 35]) are ongoing when interactions with the native oxide layer of the Si particles occur. Moreover, these surface interactions between carboxylic acids and Si particles are characteristic for both mono- and multifunctional carboxylic acids, as demonstrated by IR spectroscopy [31].

So far, IR spectroscopy has been the main technique used to study the Si-binder interface after electrode preparation [26, 28, 31, 35, 36]. However, the interactions between Si and carbonyl groups in buffered aqueous media after slurry preparation and cycling only occur in a volume around the Si particle with a few nms of thickness. Therefore, highly surface-sensitive techniques, such as photoelectron spectroscopy (PES), are the right tools to gain a more detailed surface information. Because of the SEI layer on top of cycled electrodes, the probing depth has to be significantly higher than for pristine active material powders or electrodes before cycling to gain information about the underlying SiO_2/citrate buffer/binder interface (30–50 nm instead of a few nm for pristine electrodes). To account for these different probing depth requirements, in this study we have exploited a combination of soft and hard x-ray PES (SOXPES/HAXPES) using synchrotron radiation at the Diamond Light Source (UK) that allowed us to tune the probing depth [4, 19, 37] depending on the surface characteristics of the electrode. In addition, we have conducted in-house PES experiments on buffer-treated Si powders. For cycled electrodes, this non-destructive depth profiling approach has proven to provide detailed surface information from both the topmost surface layers [5, 8, 38], i.e. SEI layer, and the underlying active material, i.e. the native Si-oxide layer and bulk Si.

The results of this study shed new light on the performance-enhancing role of citric acid as a slurry/electrode additive in Si electrodes by leveraging the high surface sensitivity of PES. The work is divided in three parts, each adding a new layer of complexity in terms of the underlying chemically and electrochemically induced surface changes. Starting with neat Si particles, treated with buffer solutions, changes at the native SiO_2 oxide layer are analysed. In a second part, pristine Si electrodes are analysed, which show altered features in their PES spectra due to the presence of carbon black and the electrode preparation process. The third part is on depth profiling of cycled electrodes, where deciphering of the buried interfaces below the SEI layer is enabled.

2. Experimental

2.1. Materials
Unless stated differently, the materials have been used as received. Silicon nanoparticles (30–50 nm, >98%) were purchased from Nanostructured & Amorphous Materials Inc. (Houston, USA). The conductive

Table 1. Sample details.

Samples	Composition	Drying conditions	Storage/handling	Measurement
Surface-treated[a]	Si	RT	Ambient	In-house
Si powder		120 °C, vacuum		
	Si + CMC–Na	RT	Ambient	In-house
		120 °C, vacuum		
	Si + buffer	RT	Ambient	In-house
		120 °C, vacuum		
	Si + CMC–Na + buffer	RT	Ambient	In-house
		120 °C, vacuum		
Pristine electrodes	Si + CB + CMC–Na	120 °C, vacuum	Glovebox	Synchrotron
	Si + CB + CMC–Na + buffer	120 °C, vacuum	Glovebox	Synchrotron
Soaked electrodes	Si + CB + CMC–Na	120 °C, vacuum	Glovebox + pouch cell	Synchrotron
	Si + CB + CMC–Na + buffer	120 °C, vacuum	Glovebox + pouch cell	Synchrotron
Cycled electrodes	Si + CB + CMC–Na	120 °C, vacuum	Glovebox + coin-cell-type	Synchrotron
	Si + CB + CMC–Na + buffer	120 °C, vacuum	Glovebox + coin-cell-type	Synchrotron

[a] Surface-treated Si samples did not contain carbon black in order to facilitate the analysis and interpretation of the spectra and receive an 'undisturbed' picture of the Si surface.

additive SuperC45 was provided by Imerys Graphite & Carbon. Carboxymethylcellulose sodium salt (CMC–Na, Lot No.: 1021813, degree of substitution: 0.82) and lithium foil (750 μm, >99.9%) was obtained from Alfa Aesar. Glassfiber separators (EUJ 116, Hollingsworth & Vose, UK) were dried prior use at 150 °C overnight under vacuum. The electrolyte comprised of 96 wt.% LP30 (1 M LiPF$_6$ in ethylene carbonate (EC): dimethylcarbonate (DMC), v/v = 1:1, BASF) and 4 wt.% fluoroethylene carbonate (FEC, BASF). Citric acid monohydrate (>99.0%) and sodium citrate tribasic dehydrate (>99.5%) were purchased from Sigma-Aldrich.

2.2. Buffer preparation
The 100 ml of a 0.1 M citrate buffer solution (pH 3) was prepared by dissolving the acid (8.2 mmol, 1.723 g) and conjugate sodium salt (1.8 mmol, 0.353 g) in deionized water.

2.3. Electrode preparation
The electrode formulation comprised of Si, SuperC45 and CMC–Na in a mass ratio of 8:1.2:0.8. For a 1 g batch 4.5–5.0 ml, deionized water or citrate buffer was used. The slurry was prepared with an ultra-turrax disperser (IKA Ultra-Turrax T25) at 16 000 rpm. First CMC–Na was dissolved and then carbon black and silicon were added. After each addition, the slurry was stirred for 2 min. A detailed description of the slurry preparation is provided elsewhere [31]. The slurry was cast on a copper foil (20 μm, Schlenk Metallfolien, Germany), and dried under ambient conditions. Electrodes were cut into discs of 13 mm in diameter, and dried overnight at 120 °C under vacuum, in the glovebox antechamber. The active material loading was around 1.5 mg$_{Si}$ cm^{-2}.

2.4. PES sample preparation and analysis
A summary of all samples, their composition and history, is provided in table 1.

2.4.1. Surface-treated Si powder
Following the procedure of the electrode preparation, Si powders were dispersed in solutions of deionized water or citrate buffer with and without CMC–Na using a planetary mixer (Thinky, ARV-310P). The components were used in the same proportions as in a regular slurry preparation and were immersed for a similar duration in the aqueous media. The suspension was then spread on copper foil using a spatula, and dried under ambient conditions. The resulting coatings were cut into discs of 12 mm. Each formulation was dried both under ambient conditions (room temperature and atmospheric pressure) and at 120 °C under vacuum overnight, respectively.

2.4.2. Pristine samples
Pristine samples were stored in an Ar-filled glovebox with the other samples, so that the electrodes are exposed to the same drying conditions as soaked or cycled samples.

2.4.3. Soaked samples

The electrodes, in order to imitate a cell stack, were stored over an electrolyte-soaked glass-fibre separator and a piece of lithium foil. The sandwich was sealed in a pouch bag, and stored with a constant stack pressure for the same duration as the electrochemical tests for the corresponding cycled samples.

2.4.4. Cycled samples

The Si–Li half-cells were cycled in a coin-cell-type setup [39]. Lithium was punched in 13 mm diameter discs. The electrodes were spaced by 3 glass-fibre separators, which were soaked by 500 μl of electrolyte (LP30 + 4 wt.% FEC). The cells were closed with a torque wrench to provide a constant and reproducible stack pressure. The cells were conditioned using an Arbin battery cycler. On the first cycle a current equivalent to C/25 (1C = 3579 mAh g^{-1}) was applied using the constant current-constant potential (CC–CP) technique (potential cut-offs, CC-step: 5 mV and 1.5 V, current cut-off, CP-step: C/50). In the subsequent nine cycles, the charging current was increased to C/10; the discharge current to C/3 (potential cut-off, CC-step: 5 mV, current cut-off, CV-step: C/20). The cells were stopped in discharged (delithiated) state.

2.4.5. PES measurements

In-house x-ray PES (Thermo Fisher Scientific, K-Alpha with a monochromated Al-Kα source, $h\nu$ = 1487 eV) experiments were conducted on surface treated Si powder. Pristine, soaked and cycled Si electrodes were examined by a combination of soft (100–1000 eV, SOXPES) and hard (2360 eV and 7080 eV, HAXPES) x-ray PES at the I09 beamline at the Diamond Light Source. The sample preparation and mounting on the sample holder was carried out in an Ar-filled glovebox. Soaked and cycled samples were washed with 2 ml DMC after cell disassembly.

Spectra were references to the hydrocarbon peak (–C–C– (sp^3)/–CH–) in the C1s spectrum at a binding energy of 285 eV. Data analysis and plotting for synchrotron data was performed in IGOR Pro (v. 6.3.7.2; WaveMetrics Inc.). In-house data was analysed using Avantage (v. 59904; Thermo Scientific). A Shirley background function was used for background subtraction. For peak fitting Voigt profiles were used with a Lorentzian contribution of 20%–30%.
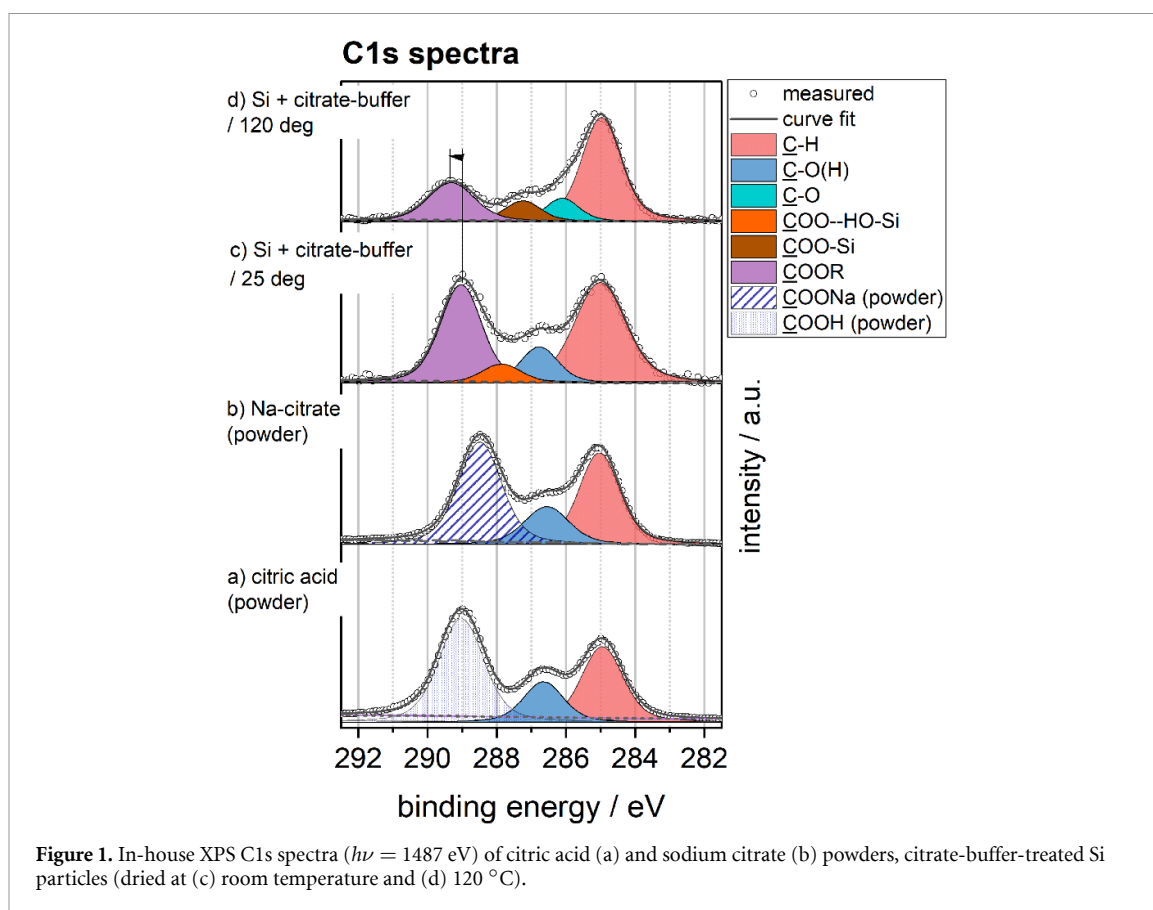
3. Results and discussion

3.1. In-house x-ray photoelectron spectroscopy (XPS) study on acid-treated Si powders

In the first section of this study, changes in the surface chemistry of buffer-treated Si nanoparticles will be discussed based on C1s in-house XPS data (photon energy Al Kα, $h\nu$ = 1487 eV). The particles were dispersed in aqueous solutions of either a citrate buffer (pH = 3), CMC–Na binder, or both the citrate buffer and CMC–Na (pH = 3); for comparison Si exposed to deionized water was used ('buffer-free' sample). A typical lab-scale slurry preparation was simulated (i.e. stirring equipment, preparation time and ratios of components, etc) and the thus prepared Si slurry was cast on Cu foil. The adhesion, even without a binder or carbon black, was sufficient to prepare electrodes for XPS analysis. One batch of each composition was additionally dried at 120 °C under reduced pressure for 12 h, which would correspond to the regular drying conditions of electrodes prior to cell assembly. As reference, the XPS spectra of citric acid and trisodium citrate powders (the two buffer components) were also recorded. A first comparison between citric acid and citrate powders, citrate-buffer-treated Si particles (dried at room temperature and 120 °C) are presented in figure 1.

Starting with the results from buffer components shown in figures 1(a) and (b), it is visible that both the citric acid (figure 1(a)) and Na-citrate powder (figure 1(b)) have similar environments for their CH$_2$-groups (sat. hydrocarbons, red peak) and their C–OH-group of the molecule (blue peak). At the same time, the signal of the carboxyl-group (COOX, X = H, Na) shifts towards lower binding energies from 289.0 eV to 288.5 eV, when the COOH-group is deprotonated because of electron delocalization.

Even if the buffer contains a mixture of both citric acid and citrate in a ratio of about 4:1, this does not seem to be directly reflected in the C1s spectra of the buffer-treated Si samples (figures 1(c) and (d)). In fact, the sample dried at room temperature (RT) (figure 1(c)) exhibits a peak at 289 eV, which can be attributed to the carboxyl-group of citric acid (in order to distinguish this component from the COOH-group of the neat citric acid, it was denoted 'COOR'). Given that the COOH peak in CitAc and the COOR peak in the buffer-treated sample (RT) exhibit the same binding energy shift, 'COOR' could be ascribed to free carboxyl-groups (as opposed to 'adsorbed' or 'tethered' groups that interact with surface groups of the native Si oxide layer [31, 35, 40]), originating from citric acid molecules located at the interface of the particles. Both peaks of the C–O(H) and C–H components are located at similar binding energies with respect to the ones of the powder samples (286.5 eV). However, the C–H component in the buffer-treated sample (RT) is broader than in the powder reference samples, which is likely due to additional contributions from C–H

Figure 1. In-house XPS C1s spectra ($h\nu = 1487$ eV) of citric acid (a) and sodium citrate (b) powders, citrate-buffer-treated Si particles (dried at (c) room temperature and (d) 120 °C).
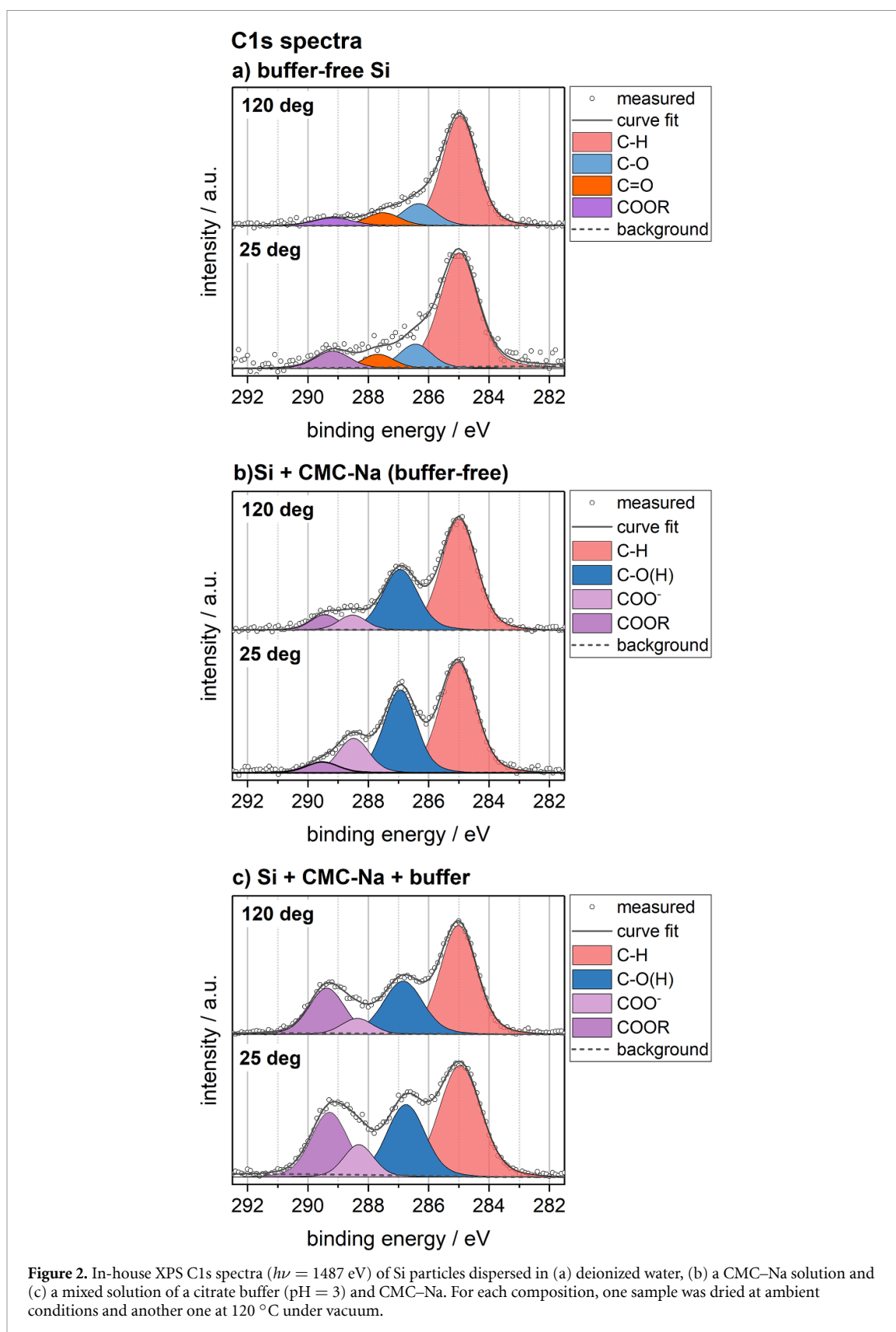
components found on the Si nanoparticle surface, as will be discussed later (figure 2(a)). In addition, a fourth component located at 287.8 eV, denoted 'COO–HO–Si', was used to fit the spectrum. Although, its assignment is questionable, we assume that it is a second carboxyl component, involved in surface interactions with Si–OH groups. This component prevents an unreasonably broad C–O peak while fitting spectra, and its presence has little effect on the neighbouring COOR component peak parameters.

Interestingly, when the sample is dried under vacuum at 120 °C, the 'COOR' peak shifts by 0.3 eV (to 289.3 eV) towards higher binding energies and, at the same time, the two smaller peaks, located between 'COOR' and 'C–H', shift towards lower binding energies by about 0.6 eV, in comparison to both the RT and the buffer-free Si samples (figure 2(a)). This can be interpreted as the formation of new surface groups, for example, adsorbed citric acid molecules could have reacted with the Si surface groups, leading to slightly altered carbon environments due to the formation of a covalent R–(C=O)O–Si– bond and hence a shift in binding energy. Such surface-tethering mechanism has been suggested for water-soluble binders in contact with Si nanoparticles during slurry preparation in previous studies [26, 28]. However, esterification and anhydride formation [31] may yield compounds or polymers in a similar binding energy range [41].

To establish the effect of drying temperature on the changes of Si surface chemistry in dependence of the slurry medium, the C1s spectra of the buffer-free Si particles, the (buffer-free) CMC–Na-treated Si particles, as well as the citrate-buffer- and CMC–Na-treated Si particles are shown in figures 2(a)–(c). Each panel shows the C1s spectra of both the sample dried at RT and the one dried at elevated temperature (120 °C under vacuum). In figure 2(a) the buffer-free Si samples are shown. The differences between the C1s spectra of the RT-dried and the heat-treated samples are comparatively small. The dominant feature in both spectra is the saturated hydrocarbon peak ('C–H') at 285 eV that is typically ascribed to carbon residues on the particle surface (e.g. from synthesis and exposure to air). The RT sample also shows a higher signal-to-noise ratio and a more intense 'COOR' peak. The vacuum drying appears to remove some of these components from the Si surface.

When Si particles are dispersed in a CMC–Na aqueous solution (figure 2(b)), two new peaks appear in the binding energy range between the C–H and COOR peaks. The spectra are dominated by new components, originating from the CMC–Na binder, specifically, a higher content of C–OH groups, represented by a strong C–O(H) signal at 286.9 eV. The carboxyl-group in the carboxymethyl moiety of CMC–Na is located at 288.5 eV, which agrees well with the binding energy determined for the COONa-group of trisodium citrate. Since the two groups appear indistinguishable from one another, we

Figure 2. In-house XPS C1s spectra ($h\nu = 1487$ eV) of Si particles dispersed in (a) deionized water, (b) a CMC–Na solution and (c) a mixed solution of a citrate buffer (pH = 3) and CMC–Na. For each composition, one sample was dried at ambient conditions and another one at 120 °C under vacuum.

have denoted them as COONa (light purple peak in figures 2(b) and (c)). In addition, a small contribution of a COOR environment (dark purple peak) was observed at 289.5 eV, similar to the COOR-components seen in the buffer-treated Si samples (figures 1(c) and (d)) and the buffer-free sample (figure 2(a)). Interestingly, when the CMC–Na-treated sample (figure 2(b)) is vacuum-dried, the relative peak area of the COONa-group decreases significantly, while a less-pronounced intensity decrease with respect to the C–H

component is also observed for the C–O signal. In contrast, the COOR peak intensity remained about constant before and after drying relative to the C–H peak.

From the comparison between the relative peak intensities of the COOR component in figures 2(a) and (b), it might seem as if the groups can be assigned to the (already) existing surface groups on the Si particles. However, the absolute peak intensities are considerably higher in figure 2(b), indicating that the signal comes mainly from the presence of the functional groups of the CMC–Na binder. The present silanol groups (Si–OH) on Si surface, in combination with COH and COONa in the binder, can lead to crosslinking reactions [30, 31, 42] and surface grafting [26, 43] under the influence of elevated temperature in vacuum conditions, which could be the cause for the changing the relative peak intensities of the COONa and C–O species between the RT-dried and heat-treated sample in the figure 2(b).
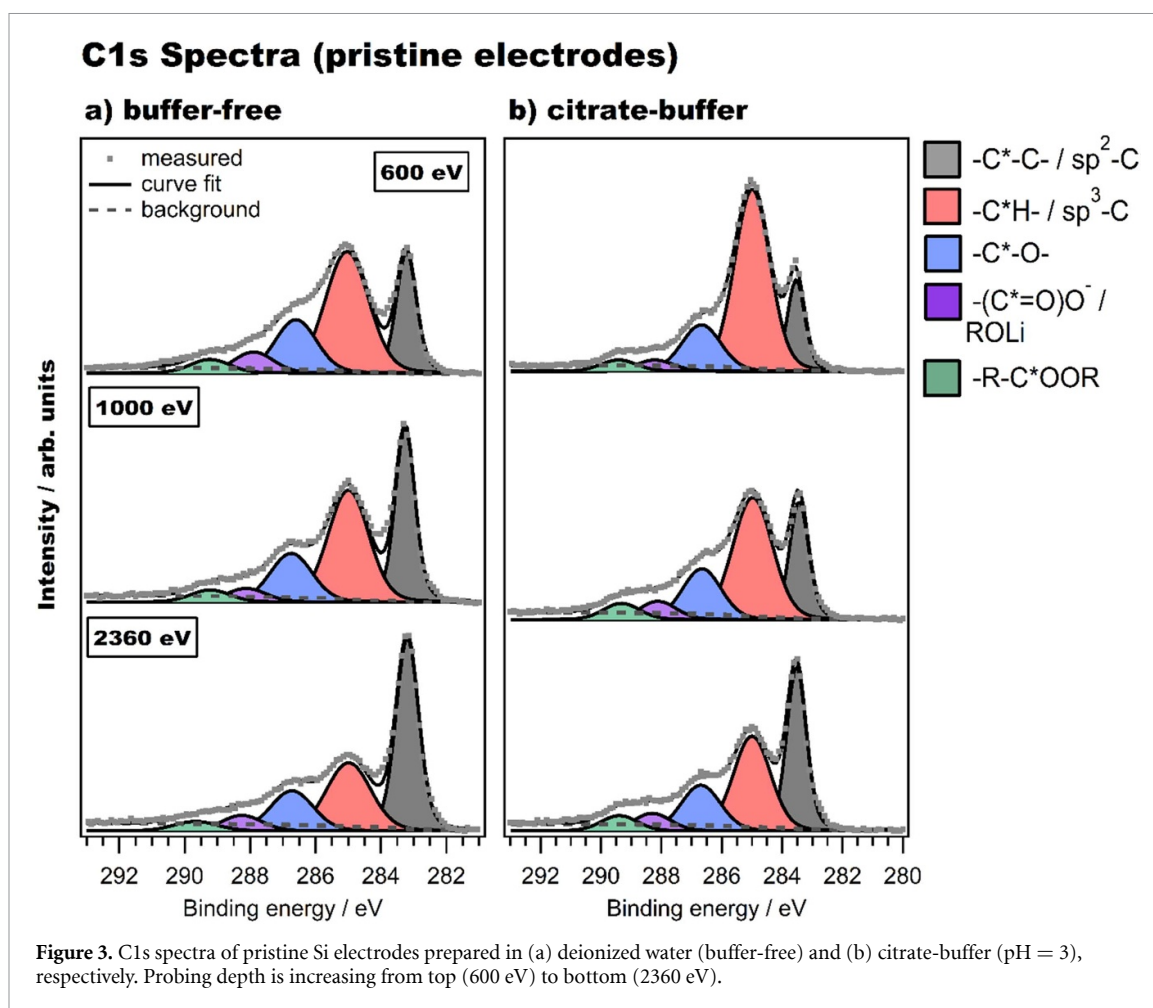
Similar trends are observed for the Si particles that were treated in a mixed solution of CMC–Na and citrate buffer (figure 2(c)). The critical difference of this mixture is that the CMC–Na binder is protonated to a significant degree (about 60%–70%; i.e. –COOH instead of –COONa), when dissolved in the citrate buffer solution [44]. Under these conditions, esterification reactions are more likely, because water is formed as a by-product, which is then removed when sample is placed under vacuum at elevated temperature, shifting the equilibrium of the reaction, as discussed in our previous study [31]. Based on this consideration, the peak at 289.5 eV, therefore, is comprised mainly of carboxyl groups (COOH) belonging to CMC–H and citric acid. Contributions from additional reacted surface species, specifically potential ester groups ('COOR'), may also be present. After drying, the area of the COOR peak has decreased but is still significantly more intense than in the case for a (buffer-free) CMC–Na-treated Si (figure 2(b)). Unfortunately, newly formed surface or crosslinking groups in figure 2(c) are masked in this spectrum because of the intense COOH-signals, as a result of the high acid concentrations. However, the relative changes in peak intensities with respect to the C–H peak (all peaks show a smaller relative peak intensity to this peak after the drying process), indicate a consumption of functional groups because of the Si-surface reactivity and crosslinking reactions.

As a final remark, it is worth noting that no changes in the native Si oxide could be observed in the Si2p spectra with an exception of the case, where Si particles were exposed to only deionized water. In this case, the SiO$_2$ peak area was slightly larger, than the SiO$_2$ signals of buffer- and/or binder-treated samples. An overlay of the four samples at both drying conditions is provided in figure S-1, showing nearly identical Si environments. The signal attenuation from samples that were exposed to buffer and/or binder is likely a result of the additional organic layer on top of the Si particles. This finding is in contrast to the original XPS analysis by Mazouzi *et al* [26], who reported a silyl-ester bond at 103.6 eV in the Si2p spectrum of a Si sample, treated in mixed citrate buffer, CMC–Na solution (as compared to a sample without the buffer component). As shown in the example spectrum in figure S-2, the Si oxide environment can be fitted adequately with one doublet peak ($\Delta = 0.63$ eV), resulting from spin-orbit splitting of the 2p orbital, with a reasonably small full-with at half maximum (FWHM) of 1.49 eV.

3.2. Depth profiling using a combined soft and hard x-ray PES (SOXPES/HAXPES) approach

The analysis of the C1s spectra have shown that buffer and binder components deposit on the Si particle surface during slurry preparation and modify the organic species on the particle surface. The Si2p spectra showed that the effects on the actual Si species in the surface region are minor. A more detailed analysis of both the surface layers and bulk components in pristine and cycled Si electrodes was carried out, exploiting the fact that probing depths can be tuned using synchrotron radiation in both the soft x-ray and hard x-ray range, i.e. either towards higher surface sensitivity or higher probing depth, thus allowing depth profiling of the SEI and underlying phases.

In general, the inelastic-mean-free-path (IMFP) of the generated photoelectrons determines the probing depth. The IMFP in turn depends on the kinetic energy of the electrons in the material, which corresponds to the difference between the excitation energy and the binding energy of the electron. Thus the probing depth depends on the excitation energy, element and orbitals [37, 45]. To probe the topmost organic layer on Si particles, low excitation energies of 1000 eV or less giving a probing depth of only a few nm are sufficient [46, 47]. Using SOXPES, the excitation energies can be readily tuned in the required range (common in-house excitation energies are 1254 eV (Mg K$_\alpha$) and 1486 eV (Al K$_\alpha$)). In this study, SOXPES was conducted in two different modes: at a constant excitation energy of 1000 eV for all elements and with a constant photoelectron kinetic energy of 300–310 eV. Since the kinetic energy of the photoelectrons varies in dependence of the element/orbital in the first approach, so does the probing depth. Using a constant kinetic energy (excitation energy is changed instead) fixes the probing depth independent of the element. For instance, the C1s environment is probed with 600 eV, while the Si2p environment is analysed with a lower excitation energy of 415 eV. In both cases, the core level photoelectrons are emitted with a kinetic energy of around 300–310 eV, giving a very high surface sensitivity and the similar probing depths.

Figure 3. C1s spectra of pristine Si electrodes prepared in (a) deionized water (buffer-free) and (b) citrate-buffer (pH = 3), respectively. Probing depth is increasing from top (600 eV) to bottom (2360 eV).

Different surface information can be further obtained from changing the probed orbitals (where possible). Specifically, higher surface sensitivity at a given excitation energy can be achieved in spectra of the Si1s orbital, as compared to the Si2p orbital, due to the vastly different binding energies (∼1840 eV vs. ∼100 eV) between the two orbitals. The binding energy of the Si1s exceeds the typical in-house excitation energies, which is why the experiments were carried out under hard x-rays (HAXPES) conditions at the Diamond Light Source (i09 endstation). The endstation offers the possibility to straightforwardly switch between soft and hard x-rays on the same sample, thus allowing a facile acquisition of information by both SOXPES and HAXPES. Therefore, a nearly non-destructive depth profile of the electrode surfaces can be performed to follow chemical gradients in the SEI and identify reaction species at the electrode/electrolyte interface.

3.3. PES study on pristine, buffer-treated Si electrode coatings

In the second part of this work we investigated pristine Si electrodes (comprised of Si nanoparticles, carbon black and CMC–Na binder), prepared either with or without the citrate buffer solution as a solvent. In other words, a complete electrode mixture was analysed, while in the previous section the system was simplified by removing CB from the sample. Using SOXPES (excitation energies < 1000 eV) the topmost surface layers are probed that include both the organic surface layer (binder and carboxylic acid), the native Si oxide as well as a contribution from underlying bulk Si (Si^0).

3.3.1. Carbon (C1s) spectra

To follow possible chemical gradients in the uncycled electrodes' surface regions, figure 3 shows the C1s spectra measured at 600 eV, 1000 eV and 2360 eV excitation energies for pristine Si electrodes prepared with and without buffer (C1s spectra measured at 7080 eV are provided in figure S-3). The corresponding peak areas (normalized by total peak area) are reported in table 2. At low probing depth (600 eV) a dominant C–H/sp^3-C peak is observed. Because of the high surface sensitivity, it is mainly the organic species on top of the active material that is visible in the C1s spectrum, i.e. binder, buffer and surface groups of CB. In addition, the presence of CB adds a new signal at around 283.3 eV, assigned to sp^2-hybridized carbon

Table 2. Comparison of peak areas of the normalized C1s spectra of pristine Si electrodes between a buffer-free and a citrate buffer-containing sample at three different excitation energies.

Peak assignments	Buffer-free			Citrate-buffer		
	600 eV	1000 eV	2360 eV	600 eV	1000 eV	2360 eV
–C–C– (sp^2)	0.222	0.326	0.451	0.161	0.232	0.347
–C–H–	0.454	0.404	0.294	0.615	0.472	0.361
–C–O–	0.190	0.180	0.166	0.172	0.190	0.182
–(C=O)O$^-$/ROLi	0.072	0.048	0.061	0.039	0.065	0.061
–R–COOR	0.046	0.042	0.040	0.039	0.058	0.057

(sp^2-C–C), indicated in grey. It is important to note that the relative peak intensities in figure 3 are not directly comparable to the ones in figures 1 and 2, as the relative peak intensities change with different probing depths (the excitation energy of in-house XPS is between 1000 eV and 2360 eV). This can be seen clearly when comparing the peak intensities of the sp^2-C and sp^3-C components: while the sp^3-C peak area peak ('saturated hydrocarbons'; red) decreases with increasing probing depth, the sp^2-C (carbon black; grey) behaves in the opposite way. Like the silicon particles, CB particles are covered with a layer of buffer and/or binder and therefore the sp^2-C signal intensity increases with probing depth. For example, in the buffer-free sample (figure 3(a)), the peak area of the sp^2-C component at 600 eV is about half the area of the sp^3-C component, while at an excitation energy of 2360 eV, the values of the normalized peak areas are reversed (table 2).

Hence, the intensity of the sp^2-C signal is a measure of the surface layer thickness on top of the CB particles. The thicker the surface layer, the weaker is the expected signal from the underlying bulk material. The changes in surface layer thickness can be expressed in terms of the CH–/sp^2-C-peak ratio at different excitation energies. For instance, in the case of the citrate-buffer-treated Si sample, the ratios are 3.82 (600 eV), 2.03 (1000 eV) and 1.04 (2360 eV) (calculated from table 2). These values are about 60%–80% higher than the ratios of the corresponding buffer-free Si electrode (2.05, 1.24 and 0.65, calculated from table 2). A thicker surface layer for buffered samples is reasonable, given that in slurries with buffer more organic material is present, depositing during the drying process on electrode components. However, it should be noted that the surface layer thickness on different electrode components may vary due to surface reactivity and therefore, the surface layer thickness on CB and Si particles might differ.

In contrast to the probing-depth-related intensity changes, it was observed that the peak intensity of the C–O species (blue) remained nearly constant independent of the probing depth and sample. Therefore, in figure 3, the relative intensity of the –C–O– peak appears to increase with respect to the sp^3-C peak that is decreasing with higher probing depth. This is an indication that within the surface layer these species are located closer to the Si and CB particle interfaces. In addition, polar surface groups on CB may contribute more to the C–O signal intensity as the probing depth increases because surface-near species make up a smaller fraction as compared to the overall probing volume, thus increasing the fraction of detectable components further beneath the surface.

Another noteworthy feature are the relative peak intensities of species found above 287 eV, i.e. mainly carbonyls and alcohols. In the CB-free samples in figures 2(b) and (c) (Si + CMC–Na and Si + buffer + CMC–Na), the intensity of these species showed clear differences between spectra of the buffer-free and buffered samples, while their intensity has strongly diminished in relation to the –C–O and –C–H– components in the CB-containing samples shown in figure 3. For example, the –COOR and –CO(H) peaks in figure 2(c) showed similar peak intensities, whereas in the pristine electrode formulation (figure 3(b)) the –COOR intensity is greatly reduced to about 25%–33% of the –C–O– signal, as can be seen in table 2.

3.3.2. Silicon (Si2p and Si1s) spectra

As stated above, the Si environment can be probed either by using the Si1s or Si2p orbitals, with different surface sensitivity, depending on the IMFP of the photoelectron [37]. This relation can be seen in figure 4(a), that shows the Si2p spectra for excitation energies of 415 eV and 1000 eV. In addition, in figure 4(b) the Si1s spectrum obtained with an excitation energy of 2360 eV is shown. The kinetic energy of the Si1s photoelectrons lies around 520 eV and thus between the kinetic energies (315 eV and 900 eV) of the Si2p photoelectrons, measured with around 315 eV and 900 eV. Because the spin–orbit coupling yields a doublet peak for p-orbitals, analysis of the Si1s signals offers an easier comparison, as only a single peak represents each of the compounds. In the Si2p spectra the peak intensities of the $Si2p_{1/2}$ and $Si2p_{3/2}$ components are coupled by a fixed ratio of 1:2 ($Si2p_{1/2}$:$Si2p_{3/2}$) and fixed binding energy difference (0.6 eV) and thus cannot be fitted independently. As can be seen in figure 4(a), for the Si^0 environment there is a deviation between measured intensity and the fitted $Si2p_{1/2}$ component that might originate from the fact that nanoparticles are

Table 3. Peak areas of the normalized Si2p and Si1s spectra (figure 4). Contributions of the $p_{1/2}$ and $p_{3/2}$ peaks were added up in the values for Si2p spectra. Suboxide contributions (red and blue peaks, figure 4) were summarized in a single value.

Peak assignments	Buffer-free			Citrate-buffer		
	Si2p, 415 eV	Si2p, 1000 eV	Si1s, 2360 eV	Si2p, 415 eV	Si2p, 1000 eV	Si1s, 2360 eV
Si^0	0.13	0.41	0.22	0.25	0.40	0.31
SiO_2	0.52	0.33	0.44	0.50	0.27	0.40
SiO_x (sum)	0.13	0.10	0.13	0.11	0.14	0.10
SiO_2-to-Si^0 ratio	4.00	0.82	2.0	2.00	0.68	1.27

investigated, as opposed to a flat and crystalline Si surfaces. Hence, the fitting constraints lead to systematic deviation from the actual peak areas for the Si^0 peak (see table 3). Using the Si1s spectra for the comparison instead avoids this problem. The (minor) contributions of suboxides (SiO_x) in the native oxide layer (indicated as the red and blue peaks) are similar in both samples (figure 4 and table 3), and are believed to be an inherent property of the Si nanoparticles, therefore, they are not considered in detail in following discussions. The changes at the Si interface can be analysed based on the relative comparison of the peak areas of the Si^0 and SiO_2 signal (table 3). The SiO_2-to-Si^0 ratios for 415 eV (Si2p) and 2360 eV (Si1s) suggest that the SiO_2 signal is stronger in the buffer-free electrode. The fact that these differences are seen only in measurements with the highest surface sensitivity (SOXPES for Si2p and HAXPES for Si1s) suggests that probing the Si2p environment with in-house instrumentation (figure S-1) does not provide sufficient surface sensitivity to observe clear differences between a buffer-free and a buffer-treated Si surface.
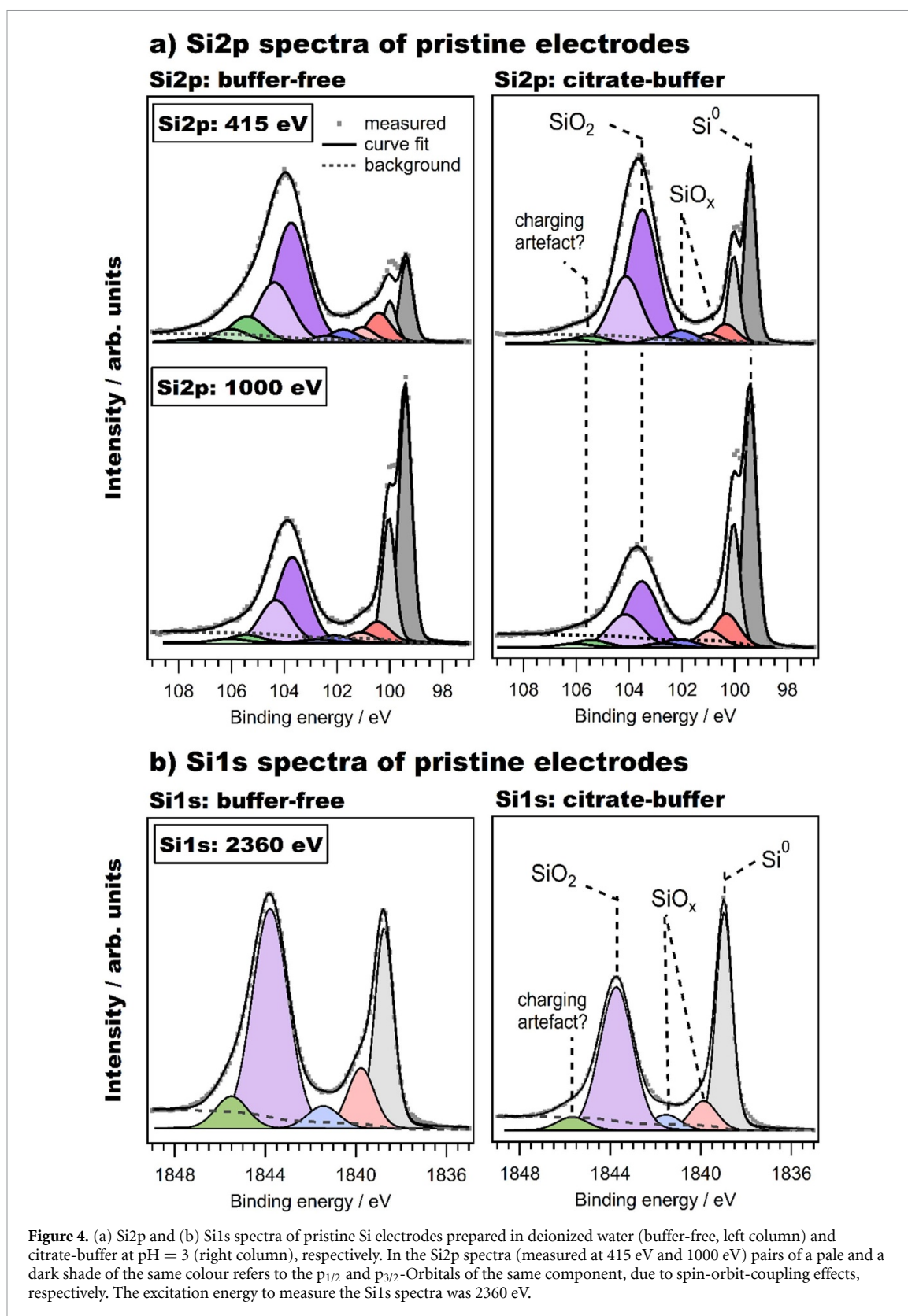
    A comparison between the SiO_2-to-Si^0 ratios of buffer-free and buffer-containing samples suggests a thicker SiO_2 layer in samples prepared without buffer at around pH 7. In fact, Si nanoparticles react with water during the slurry preparation, resulting in H_2 evolution. We have demonstrated the H_2 gas evolution in our system in part 1 of this study [48], where the gas evolution increased when a citrate buffer is used instead of water. As described by both Hays *et al* [49] and Rodrigues *et al* [50], the gas evolution is strongly pH dependent and is significantly amplified when conductive carbon materials are present. This reaction drives the growth of the SiO_2 layer on the Si surface. A comparison between our previously discussed in-house XPS results on samples without carbon black (figures 1, 2 and S-1) and the Si spectra of electrode composites, presented in figure 4, generally supports the conclusion that the mere addition of carbon black alters the SiO_2 layer of the active material. Furthermore in another study, Touidjine *et al* [51] demonstrated that the exposure of Si particles to water does not only trigger surface reactions and SiO_2 formation, but also leads to an increase in surface area due to the fact that this process results in a more porous SiO_2 layer. Because of the comparatively short water exposure of around 30 min, mimicking typical lab-scale processing times (compared to several hours or days in previous works), differences between the two samples might be more subtle in our example than described in literature. When considering the SiO_2-to-Si^0 ratio, attention also has to be paid to the fact that additional surface layers, e.g. binder and/or buffer deposits, can affect this parameter, if the surface layer thicknesses are notably different. This is due to the fact that the signal intensity decays exponentially as a function of distance from the surface.
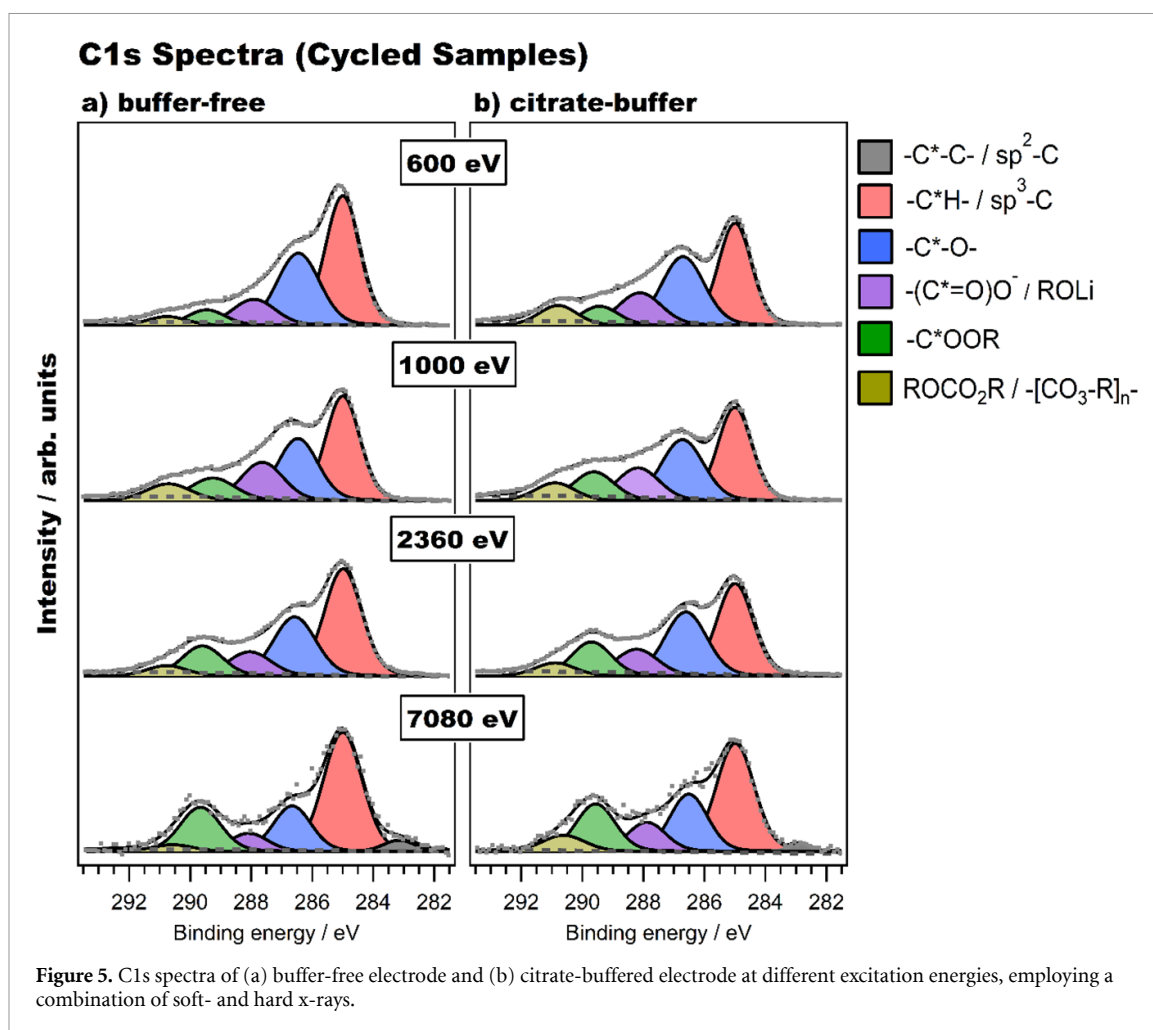
3.4. PES depth profiling on cycled Si electrodes

When Si electrodes are stored at open circuit voltage (OCV) or cycled in the carbonate electrolyte (here LP30 + 4 wt.% FEC) against metallic Li, new surface layers form. In the following, we will mainly focus the discussion on the SEI layer compositions of cycled electrodes and the influence of electrode preparation in a buffered, low pH medium.

3.4.1. OCV samples

A complete set of spectra is provided in the supporting information (figures S-5(a)–(d), while here we discuss only the most important findings. In the case of OCV samples, their surface layers tend to be thin, as the sp^2–C–C carbon black signal in the C1s spectrum and the Si^0 signal in the Si2p/Si1s spectra are still clearly visible. The major change in the spectra from the pristine electrodes, shown in the C1s spectra in figure 3, are increased amounts of oxidized carbon species. In buffer-free samples, the –C–O– peak is more intense than the –C–H– peak at the very surface, probed with excitation energy of 600 eV. In contrast, in the citrate-buffered sample the –C–O– species remain considerably less intense. Comparing the –C–O– and –C–H– intensities in figures 3(b) and S-5(a), it is apparent that both signals became weaker with respect to the sp^2–C–C peak of CB, which indicates that some of the buffer component start to dissolve in the electrolyte (as mentioned above). In both samples, the –COO^-/ROLi and –COOR species gained intensity with respect to the sat. hydrocarbon signal. The intensity changes in the higher binding energy regions of the C1s spectrum typically indicate electrolyte degradation processes. In half-cell configurations, this is often a

Figure 4. (a) Si2p and (b) Si1s spectra of pristine Si electrodes prepared in deionized water (buffer-free, left column) and citrate-buffer at pH = 3 (right column), respectively. In the Si2p spectra (measured at 415 eV and 1000 eV) pairs of a pale and a dark shade of the same colour refers to the $p_{1/2}$ and $p_{3/2}$-Orbitals of the same component, due to spin-orbit-coupling effects, respectively. The excitation energy to measure the Si1s spectra was 2360 eV.

result of 'cross-talk' phenomena of compounds that decomposed at the Li counter electrode but entered the electrolyte and deposited on the Si electrode surface. No signs of Si etching (Si2p and Si1s; figure S-5(b)) became apparent during the storage time. Phosphorous (P2p and P1s spectra; figure S-5(c)) is only found in trace amounts on the electrode surface and the main fluorine (F1s, figure S-5(d)) signal originates from surface-adsorbed or ionically-bound PF_6^- salt residues.

Figure 5. C1s spectra of (a) buffer-free electrode and (b) citrate-buffered electrode at different excitation energies, employing a combination of soft- and hard x-rays.

3.4.2. Carbon (C1s) spectra of cycled Si electrodes

The carbon environment was probed with four different excitation energies, namely 600 eV and 1000 eV (soft x-rays), as well as 2360 eV and 7080 eV (hard x-rays). Figure 5 shows the respective C1s spectra of the buffer-free and citrate-buffered electrode formulations after ten cycles. Typical for C1s spectra of cycled electrode surfaces is a dominant hydrocarbon peak (red, –CH–/sp^3-C). In this case, the origins of the peak lie in the deposition of electrolyte degradation products on the electrode surface, whereas in the previous C1s spectra of the pristine (figure 3) and OCV (figure S-5(a)) samples, the origin of the hydrocarbon species was attributed mainly to groups in the binder and buffer. Also characteristic for electrolyte degradation is an intensity increase (compared to pristine or OCV samples) of more polar species, i.e. –C–O– (blue) at 286.5 eV, carboxylates and alcoholates (R–COO$^-$/ROLi, purple, around 287.7 eV), carbonyls (esters, anhydrides, etc, –COOR, green, 289.5 eV), as well as (poly)carbonates (ROCO$_2$R/–[CO$_3$–R]$_n$–, dark yellow, 290.6 eV). From the four selected excitation energies, only the highest one provides a probing depth large enough to penetrate the SEI completely. At excitation energy of 7080 eV, the sp^2-C–C– signal of carbon black is seen, which suggests a comparatively thick SEI of an estimated 40–50 nm [52]. The signal is weaker (about half the intensity) in case of the citrate-buffered formulation, as indicated in table 4, thus indicating a slightly thicker SEI than for the buffer-free electrode.

The relative peak area ratios (table 4) show a dependence on probing depth for excitation energies between 1000 eV to 7080 eV. The values for the spectra recorded at 600 eV break with the general trend for species at higher binding energies, presumably due to the shallow probing depth (and thus disproportional changes to the chemical composition in the probing volume). In accordance with previous studies [53], it is generally found that inorganic carbonate and oxide species are located closer to the SEI–electrode interface (i.e. the inner SEI), while organic SEI components are more commonly found in surface-near (i.e. outer) regions of the SEI layer. The relative peak areas of the –CH–/sp^3-C and –COOR increase with increasing excitation energy. Carbonyls can originate for instance from esterification reactions between the carboxylic acid and the Si-surface or with the binder, but are also formed in the 'regular' electrolyte degradation process. The –C–O– and –(C=O)O$^-$/ROLi signals on the other hand were found to decrease with increasing

Table 4. Relative peak areas (i.e. $A_{peak}/A_{tot.area}$, in %) with respect to the total peak area of the C1s spectrum of the buffer-free Si and the citrate-buffered electrode formulations, in dependence of excitation energy (600 eV, 1000 eV, 2360 eV, 7080 eV).

Peak assignments	Buffer-free				Citrate-buffer			
	600 eV	1000 eV	2360 eV	7080 eV	600 eV	1000 eV	2360 eV	7080 eV
$-C-C-/sp^2$-C	0.0%	0.0%	0.0%	3.6%	0.0%	0.0%	0.0%	1.7%
$-C-H-/sp^3$-C	47.0%	39.5%	42.9%	47.6%	37.0%	35.1%	37.4%	40.1%
$-C-O-$	31.7%	31.1%	26.7%	17.8%	31.5%	28.4%	30.0%	21.1%
$-(C=O)O^-$/ROLi	11.5%	14.1%	11.1%	7.1%	15.1%	15.2%	12.6%	10.8%
$-COOR$	6.0%	9.5%	13.0%	18.4%	7.7%	12.9%	15.2%	18.0%
$ROCO_2R$ /$-[CO_3-R]_n-$	3.4%	6.2%	4.4%	2.7%	8.1%	7.8%	5.8%	6.6%

probing depth. The initial presence of carboxylic acid in the citrate-buffered electrode does not affect this general trend, which is reasonable, given the SEI layer is considerably thicker than the surface layer formed by the buffer itself during the electrode preparation.

A major reason for the similarities in the SEI composition is the use of the electrolyte additive FEC [54], as the primary SEI builder. One of the reaction pathways of FEC leads to polycarbonates ($-[CO_3-R]_n-$), e.g. poly-VC [55, 56], which is indicated by the small signal at the highest binding energy (BE) at around 290.6 eV (dark yellow peak). The signal intensity remains about constant within a margin of 2% across different probing depths, indicating their comparatively even distribution throughout the SEI. Moreover, table 4 suggests that the (poly)carbonate content in the SEI is slightly higher for the citrate-buffer sample, which could be beneficial for the long-term stability of the cell. It is possible that the buffer facilitates or assists the decomposition reaction of FEC in the early stages of SEI formation.

3.4.3. Si2p and Si1s spectra of cycled Si electrodes
Si2p spectra were recorded up to an excitation energy of 2360 eV. The spectra provided in figure S-4(a) suggest that the probing depth up to 1000 eV was not sufficient to penetrate all the way through the SEI layer and thus have been excluded from the following discussion. Spectra recorded at excitation energy of 2360 eV for cycled electrodes still show a comparatively poor signal-to-noise ratio, but three distinct peaks of the buried Si particles are distinguishable, the same applies to the Si1s spectra at 2360 eV that are provided in figure S-4(b).

The following discussion on the Si spectra of cycled samples, therefore, focuses on the HAXPES measurements at 2360 eV (Si2p) and 7080 eV (Si1s), shown in figures 6(a) and (b) (note the different probing depths in Si2p and Si1s spectra). To follow the peak assignments, the Si2p and Si1s spectra of the OCV samples are also shown for comparison in figure 6. The binding energy positions in the Si2p spectra of the OCV samples generally agree well with previously reported values for Si electrodes (similar components and composition) and also match the features of an undoped silicon wafer [4]. The bulk Si peaks (Si^0), indicated in grey, of the buffer-free OCV sample in figure 6(a) are found at 99.7 eV ($Si2p_{3/2}$) and 1838.8 eV (Si1s), respectively; the corresponding silicon oxide (SiO_2) peaks, indicated in purple, are ascribed to the signals at 104.2 eV ($Si2p_{3/2}$) and 1843.9 eV (Si1s). The peaks of the citrate-buffered OCV sample (figure 6(b)) show slightly lower binding energies in the Si2p spectrum, i.e. 99.2 (Si^0) and 103.4 (SiO_2). In addition, all spectra exhibit a suboxide component (SiO_x) at 0.8 eV higher binding energy than the Si^0 peak, indicated in red.

In the spectra of the cycled samples (figures 6(a) and (b)) the BEs of the SiO_2 peaks remain nearly the same in both samples. While the bulk Si^0 peak is clearly visible in the Si1s spectra, it is more difficult to pinpoint this signal in the corresponding Si2p spectra because of the weak intensity and the poor signal-to-noise ratio at the given probing depth. Compared to the OCV samples, the bulk Si^0 peaks for the cycled samples exhibit a shift towards lower BE in both the Si1s and Si2p spectra for both electrode preparation methods. These BE shifts can arise from the referencing to the $-C-H-$ peak in the respective C1s spectrum. In a cycled sample, the CH-peak is an SEI component that typically does not align to the Fermi level of the underlying electrode material that is part of the percolated electronic network. Thus SEI components can be shifted on the BE scale, relative to signals of the underlying active material [57]. Pristine and OCV samples are typically less affected due to the comparatively thin surface layers. In our experiments, the shift was most pronounced at 2360 eV excitation energy. In addition, amorphization of the crystalline Si particles occurs on the first cycles, which may result in slightly different Si environments.

At BEs of about 1.6–1.8 eV below the bulk Si^0 peak, a new prominent component is observed (indicated in yellow), with a binding energy of 96.8 eV ($Si2p_{3/2}$) and 1836.7 eV (Si1s), respectively. According to Philippe *et al* [8] and Lindgren *et al* [58], this signal corresponds to lithium silicides, Li_xSi. The position of this peak may depend on the degree of lithiation and is thus subject to changes for different samples. The fourth component in the cycled spectra, located at 100.1 eV ($Si2p_{3/2}$)/1840.5 eV (Si1s), indicated in dark red,
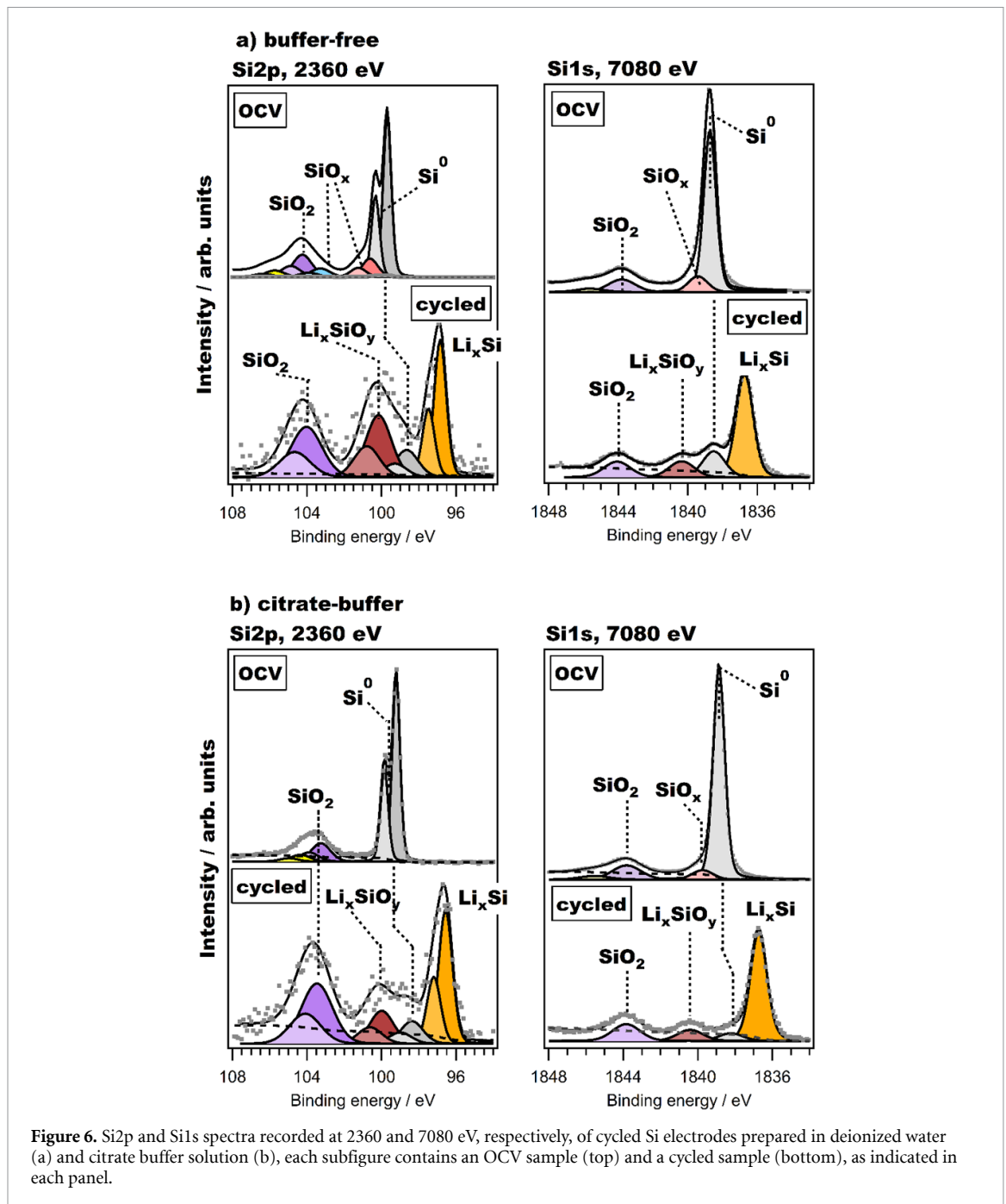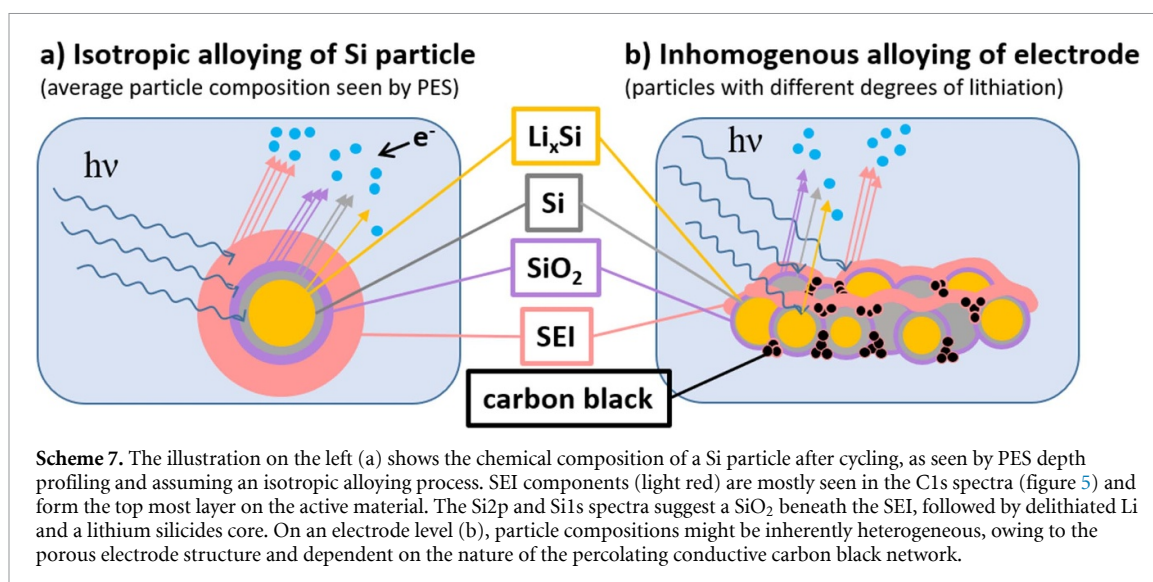
Figure 6. Si2p and Si1s spectra recorded at 2360 and 7080 eV, respectively, of cycled Si electrodes prepared in deionized water (a) and citrate buffer solution (b), each subfigure contains an OCV sample (top) and a cycled sample (bottom), as indicated in each panel.

is assigned to lithium silicates with a general composition of Li_xSiO_y (e.g. Li_4SiO_4), as suggested elsewhere [5, 8].

In summary, four main components were clearly identified in Si spectra by PES: silicon oxide (SiO_2), lithium silicates (Li_xSiO_y), elemental Si (Si^0) and lithium silicides (Li_xSi). Leveraging the different depth information of Si1s and Si2p spectra, the spatial particle (or electrode) composition can be described in more detail under certain assumptions. In scheme 7, two scenarios are illustrated, which will be referred to as homogeneous Si particle alloying and inhomogeneous (de)alloying of Si particles or Si electrodes:

Assuming isotropic particle alloying, as proposed for example by Trill *et al* [59] or McDowell *et al* [60], the particle morphology of the cycled electrode would correspond to a multi-layer core–shell-type particle with the SEI layer as the outermost layer (scheme 7: *homogeneous particle alloying*). Judging from the Si2p spectra at lower excitation energies (i.e. 415 eV or 1000 eV shown in figure S-4(a), the SiO_2 signal is the only distinguishable feature, indicating it is the first (or outermost) particle layer. This would imply that the alloying reactions occur beneath the native SiO_2 layer. The alloying of Si with Li can lead to Li_ySiO_x compounds at the SiO_2/SiO_x–Si interface, forming an additional layer between the native SiO_2 layer and the particle core, comprising the active phases of Si^0 and Li_xSi that participate in the cell reactions. From the

Scheme 7. The illustration on the left (a) shows the chemical composition of a Si particle after cycling, as seen by PES depth profiling and assuming an isotropic alloying process. SEI components (light red) are mostly seen in the C1s spectra (figure 5) and form the top most layer on the active material. The Si2p and Si1s spectra suggest a SiO_2 beneath the SEI, followed by delithiated Li and a lithium silicides core. On an electrode level (b), particle compositions might be inherently heterogeneous, owing to the porous electrode structure and dependent on the nature of the percolating conductive carbon black network.
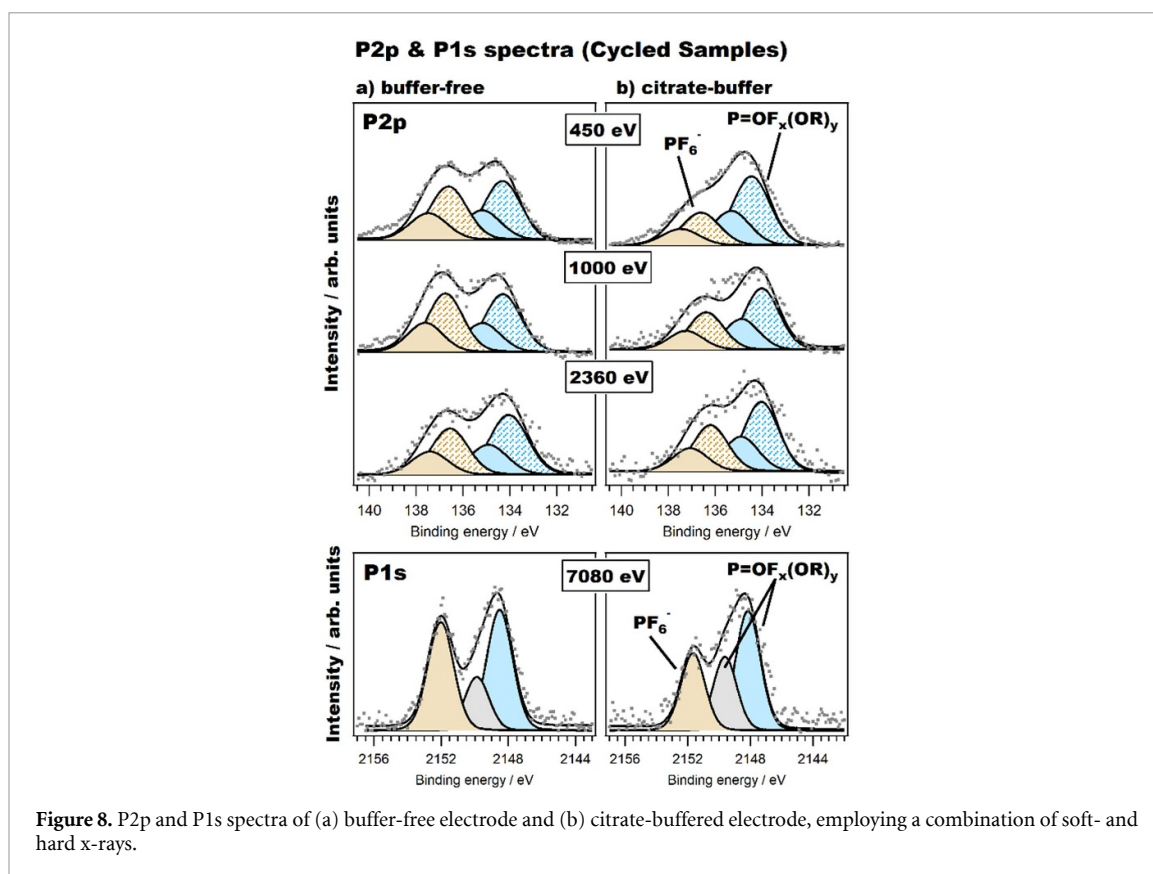
measurements at only one particular state of charge, the role of Li_ySiO_x is not entirely clear. Gradual growth of this layer may also lead to a slow consumption of the native oxide layer and may also represent an additional diffusion barrier for Li-ions in and out of the particle. A layered model stands and falls with an isotropic alloying process, i.e. the formation of core–shell-like particles. As Trill *et al* [59] found using solid-state NMR, Si particles with average diameters of 100–200 nm form an estimated 30–40 nm-thick reaction zone during the alloying reaction, and as the Si nanoparticles in this study are considerably smaller (30–50 nm particle size), they hence fall in the same size-range as the reaction zone. Unlike NMR, PES is not probing the entire bulk of the particle: the penetration depth at an excitation energy of 7080 eV is estimated to about 40–50 nm [52], which also includes the SEI layer on top of the Si particles. It is thus likely, that the highest penetration depth does not reach all the way to the particle's centre.

Another possible scenario would be inhomogeneous alloying on electrode level. It is important to recall the limitations of PES for this discussion: because PES only provides an average composition over the entire probing volume, there is a possibility that grains with different compositions (SiO_2, Li_xSi, Si^0, etc) are present within the same probing volume or that the electrodes comprise a mixture of delithiated and lithiated Si particles (scheme 7: *inhomogeneous electrode alloying*). The latter relates to increasing internal resistances in course of SEI formation and growth that can be associated with particle/domain isolation [6]. Particle rearrangements in the electrode have been reported to isolate subdomains of the electrode as well [3, 29]. Moreover, the degree of lithiation may change along the electrode cross-section, i.e. from the electrode surface (the part which is analysed by PES) towards its interface with current-collector, the alloying process becomes increasingly inhomogeneous as a result of mass transport limitations in the porous network, particularly when the pore size and its volume decreases because of SEI growth [61]. As a result, Li-richer alloys are more likely to form on average at the electrode surface towards electrolyte rather than at the current-collector interface, where the Li-ion flux might be lower.

3.4.4. P2p and F1s spectra

One of the main practical questions we aimed to answer is whether the acidic protons of the buffer induce more salt decomposition. The relative ratio of phosphorous compounds in the P2p and P1s spectra of the cycled electrodes, displayed in figure 8, allow a straightforward basis for comparison. The P2p environment was recorded for excitation energies between 450 eV and 2360 eV. For the highest excitation energy (7080 eV), the P1s environment was chosen for its better signal-to-noise ratio. In addition, it is easier to identify different species in a P1s spectrum, since each of the species is represented by a single peak rather than a doublet (analogous to Si2p/Si1s above). While the P2p spectra are fitted by only two main species, i.e. the P–F bonding of the PF_6^- anion (light brown) and alkyl fluorophosphates ($O{=}PF_x(OR)_y$, light blue), it is possible to distinguish a third component in the curve fits (indicated as grey peak) of the P1s spectrum. Assuming the binding energy is a function of the number of P–F bonds, then the two peaks at 2148 eV and 2149.5 eV can be ascribed to dialkyl monofluorophosphate ($O{=}PF_1(OR)_2$) and the monoalkyl difluorophosphate ($O{=}PF_2(OR)$), respectively. Both P2p and P1s data show that the SEI of the citrate-buffer-containing electrode has more degraded phosphate species than buffer-free one, when comparing the relative peak intensities between the PF_6^- and $O{=}PF_x(OR)_y$ signals. The latter are typically

Figure 8. P2p and P1s spectra of (a) buffer-free electrode and (b) citrate-buffered electrode, employing a combination of soft- and hard x-rays.
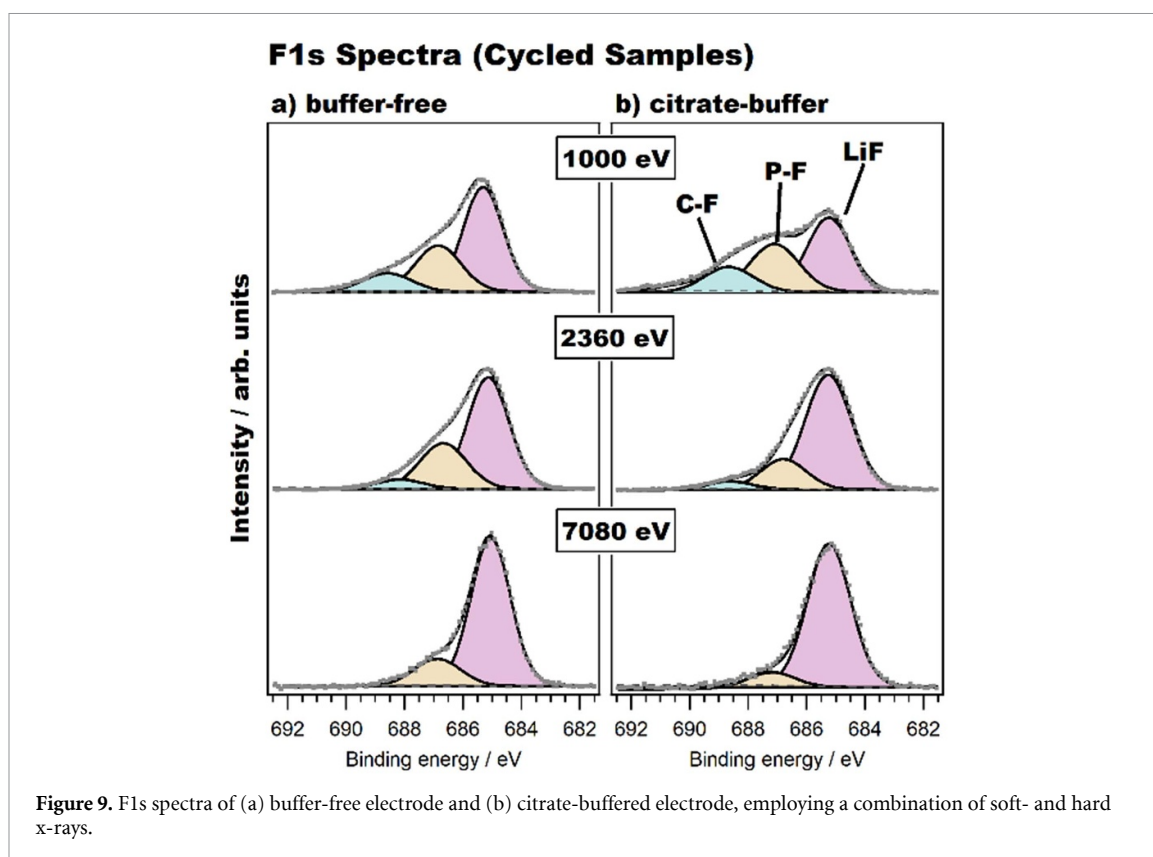
formed during the thermal decomposition of LiPF$_6$ into LiF and PF$_5$, which triggers an autocatalytic decomposition of electrolyte components [62, 63]. Another pathway to fluorophosphates is the presence of acidic protons in the electrolyte mixture that have been reported to produce POF$_3$ and PF$_5$ [64]. Although slightly higher relative contents of alkyl fluorophosphates were found for the electrode that was prepared with citric acid, the XPS data presented in figure 8 generally suggests that acid-induced degradation processes are minor. This finding is in general agreement with the absence of any POF$_3$ traces from our online mass spectrometry (OEMS) measurements in part 1 of this study [48].

The F1s spectra recorded at the excitation energies of 1000 eV, 2360 eV and 7080 eV are shown in figure 9. The most dominant peak across all excitation energies is the characteristic LiF signal at 685 eV, independent of the electrode preparation, and originates from both the degradation of PF$_6$-salt to LiF and alkyl fluorophosphates, and from FEC degradation processes [55, 56, 65]. It is therefore difficult to associate differences in the F1s spectra of the two electrode formulations directly to electrolyte salt degradation, as LiF is formed through several reactions. The fluorophosphates (both PF$_6^-$ and O=PF$_x$(OR)$_y$) described above are summarized in a single P–F component (indicated in light brown) due to their very similar BE. In addition, a peak at 689 eV (C–F, cyan) is observed, that is assigned to (organic) alkylfluorides [38], resulting from degradation processes of FEC. Another possibility for this effect is prevalent charging effects due to high photon flux at the synchrotron for the lower excitation energies.

When comparing the F1s spectra of the buffer-free and the citrate-buffer treated electrode, it is clear that the LiF peak becomes more dominant in the spectrum with increasing probing depth, suggesting higher LiF contents in the inner SEI layer, i.e. at the SEI-Si-particle interface. Both the P–F and C–F peaks are strongly dependent on the excitation energy, i.e. are unevenly distributed within the SEI thickness. The C–F peak is considerably weaker at an excitation energy of 2360 eV than at a shallow probing depth (1000 eV), while at 7080 eV it is not visible anymore. Similarly, it would appear that the P–F components accumulate mostly in the topmost layers of the SEI, as the signal rapidly decreases as the probing depth increases.

There is a clear difference in the F1s spectra at 2360 eV and 7080 eV between the two electrode formulations. The LiF peak is more dominant with respect to the P–F peak when the citrate buffer is present in the electrode formulation. As stated above, the LiF concentration can be increased by degradation of both FEC and PF$_6^-$. Although the P2p spectra suggest a tendency to produce a somewhat larger fraction of degraded electrolyte salt products when using the citrate-containing electrodes, we suspect that the main

Figure 9. F1s spectra of (a) buffer-free electrode and (b) citrate-buffered electrode, employing a combination of soft- and hard x-rays.

fraction of the signal is a result of FEC decomposition. In our OEMS study (part 1 [48]), we have already shown a notable FEC reduction in the potential region between 1.0 and 1.5 V, which is confirmed in figure 9 by the presence of C–F compounds. It was proposed previously, that trace amounts of HF could be scavenged by carboxylate groups (from the electrochemical reduction of the acidic protons above 1 V) through the following reaction (equation (1)) [66]

$$- \text{COOLi} + \text{HF} \rightarrow -\text{COOH} + \text{LiF}. \tag{1}$$
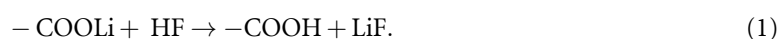
This is consistent with the slightly increased amounts of alkyl fluorophosphates observed for the citrate-buffered sample in figure 8.

4. Summary

In a first part of this study, deposition effects of CMC–Na and citrate buffer, as well as of a mixture of both components on silicon nano-powder were investigated using in-house PES. The C1s spectra of the respective organic coatings on the Si surface were distinguished from one another, and additionally changes that they undergo during typical electrode drying conditions (120 °C and vacuum) were identified. Both CMC–Na and citrate buffer treated surfaces showed the formation of new or altered carbon environments at high binding energies, suggesting surface reactions during the drying step. In the mixture of buffer and binder, these changes were difficult to separate due to two strong signals from –COOH groups (mostly citric acid, but also the protonated carboxymethyl moieties) and from –C–O–.

In the second part, where the C1s spectra of pristine Si electrodes that also comprise carbon black were studied, the C1s signals of binder and buffer appear attenuated, due to the characteristic signals of carbon black, dominated by the –C–C– and –C–O– environments. Despite the clear differences shown between a Si surface covered only with CMC–Na and a mixture of CMC–Na and citrate buffer in the first part of the study, the C1s spectra of the pristine electrodes have nearly lost all unique features, induced by the surface treatments. However, by comparison of the relative –C–H–/–C–C– peak ratio, it can be concluded that a thicker surface layer has formed when a citrate buffer was used during the slurry preparation. This finding is a strong indication that the carboxylic acid covers the particle surface, and becomes an integral part of a surface coating after slurry preparation and casting. By extension, this layer may be rendered an

'artificial-SEI' layer, when the electrode is cycled. A previous work by Nguyen *et al* [66] highlighted, for example, that the hydrogen reduction reaction of the acidic –COOH groups yields a protective carboxylate layer on the particle surface. The data of the corresponding Si2p and Si1s environments further suggests that the Si oxide layer thickness is changed when the suspension also contains carbon black, as opposed to just binder or buffer, as shown in first part concerning CMC–Na and citrate buffer treatments. In comparison with the buffer-free sample, the electrode prepared at pH 3 appeared to exhibit a thinner or possibly more porous surface layer leading to a larger contribution of the bulk Si signal (Si^0) to the spectra.

In the last part, cycled Si electrodes were characterized by a depth-profiling approach using different excitation energies to modulate the IMFP of the photoelectrons and thus the probing depths. After ten cycles, the SEI layer has reached a thickness between 40 and 50 nm [37]. A complete penetration of the SEI was only observed for the measurements with the highest excitation energy. The use of the electrolyte additive FEC generated similar C1s spectra. However, electrodes prepared with the citrate buffer exhibited a smaller hydrocarbon (–C–H–) signal contribution to the total C1s signal, while carbonates ($ROCO_2R$/–$[CO_3R]_n$–) were more prominent in this sample in deeper layers of the SEI, i.e. closer to the electrode surface. The carbonate species were mainly ascribed to poly-VC formation during FEC reduction. Analysis of the underlying Si particles was only possible using excitation energies of 2360 eV and 7080 eV (HAXPES). Although in delithiated state, cycled Si electrodes showed a strong lithium silicides (Li_xSi) peak, along with a signal for SiO_2, lithium silicates (Li_ySiO_x) and bulk Si^0. The results suggest that the particle core still contained Li_xSi, assuming isotropic particle alloying and thus a layered, core–shell-like, particle structure, with SiO_2 and Li_ySiO_x forming the outer layers. A Si phase is suspected to be in the volume between the Li_xSi core of the particle and outer layers, based on the relative intensity evolution during depth profiling. For the citrate-buffer formulation a higher SiO_2 fraction was found, indicating the native oxide layer has aged to a lesser degree, e.g. by surface etching [4, 8]. It is further important to note that the observed differences in content of Si^0 and Li_xSi in the bulk particles are an average value over all particles within the probing area. Hence, different degrees of lithiation may arise simply from inhomogeneous (de)alloying of active material or electrode subdomains (as illustrated in scheme 7) on the electrode level, which can be attributed for instance to local differences in the conductive percolated particle network. Moreover, analysis of the P2p and F1s spectra of the cycled electrodes indicates that the presence of citric acid at the electrode interface appears to have merely a minor effect on the content of salt decomposition products in the SEI layer, which is in accordance with the OEMS findings presented in part 1 of this study [48]. Although a quantification of the individual components was not possible with our synchrotron data, comparison between the F1s spectra of the cycled buffer-free and citrate-containing samples, showed the presence of slightly larger relative amount of LiF compared to electrolyte salt components (P–F) in the buffered electrode formulation.

5. Conclusion

Our PES study provided a detailed picture of the citrate-buffer treatment effects on the surface chemistry of silicon particles. Overall, we showed that both citric acid and CMC–Na binder interact with the silicon surface. After the electrode drying process, new surface groups are formed that may indicate tethering to the silicon surface or crosslinking of citric acid and the binder. While neat Si particles do not appear to be affected by the low pH buffer, changes of the native oxide layer are found after slurry preparation in the aqueous suspension with carbon black. The electrode prepared in a buffered environment tends to form thicker surface layers in contact with electrolyte, both for the pristine electrode (only buffer + binder) and the cycled electrode (after SEI formation). At the SEI-Si-particle interface, layers of SiO_2, Li_ySiO_x, Si, and Li_xSi are found, suggesting that the delithiation process is not complete. Based on the PES spectra, the particle core is comprised of Li_xSi, and thus partly remained in a lithiated state. Last but not least, the presence of acidic protons does not appear to promote accelerated electrolyte salt decomposition.

To conclude, according to our results, the citrate-buffer can extend the cycle-life of Si containing anodes as it becomes incorporated into the surface layer of the silicon particles together with the binder and creates an artificial SEI during electrode preparation and drying.

Data availability statement

The data that support the findings of this study are available upon reasonable request from the authors.

Acknowledgments

ORCID iDs

Fabian Jeschull ⬤ https://orcid.org/0000-0002-5927-1978
Hieu Quang Pham ⬤ https://orcid.org/0000-0001-8501-5815
Ahmad Ghamlouche ⬤ https://orcid.org/0000-0002-3345-7918
Pardeep K Thakur ⬤ https://orcid.org/0000-0002-9599-0531
Sigita Trabesinger ⬤ https://orcid.org/0000-0001-5878-300X
Julia Maibach ⬤ https://orcid.org/0000-0003-1339-7804

References

[1] Obrovac M N and Chevrier V L 2014 Alloy negative electrodes for Li-ion batteries *Chem. Rev.* **114** 11444–502
[2] Beattie S D, Larcher D, Morcrette M, Simon B and Tarascon J-M 2008 Si electrodes for Li-ion batteries—a new way to look at an old problem *J. Electrochem. Soc.* **155** A158–68
[3] Nguyen B P N, Gaubicher J and Lestriez B 2014 Analogy between electrochemical behaviour of thick silicon granular electrodes for lithium batteries and fine soils micromechanics *Electrochim. Acta* **120** 319–26
[4] Jeschull F, Lindgren F, Lacey M J, Björefors F, Edström K and Brandell D 2016 Influence of inactive electrode components on degradation phenomena in nano-Si electrodes for Li-ion batteries *J. Power Sources* **325** 513–24
[5] Lindgren F, Xu C, Maibach J, Andersson A M, Marcinek M, Niedzicki L, Gustafsson T, Björefors F and Edström K 2016 A hard x-ray photoelectron spectroscopy study on the solid electrolyte interphase of a lithium 4,5-dicyano-2-(trifluoromethyl)imidazolide based electrolyte for Si-electrodes *J. Power Sources* **301** 105–12
[6] Oumellal Y, Delpuech N, Mazouzi D, Dupré N, Gaubicher J, Moreau P, Soudan P, Lestriez B and Guyomard D 2011 The failure mechanism of nano-sized Si-based negative electrodes for lithium ion batteries *J. Mater. Chem.* **21** 6201
[7] Philippe B, Dedryvère R, Gorgoi M, Rensmo H, Gonbeau D and Edström K 2013 Role of the LiPF$_6$ salt for the long-term stability of silicon electrodes in Li-ion batteries—a photoelectron spectroscopy study *Chem. Mater.* **25** 394–404
[8] Philippe B, Dedryvère R, Gorgoi M, Rensmo H, Gonbeau D and Edström K 2013 Improved performance of nano-silicon electrodes using the salt LiFSI—a photoelectron spectroscopy study *J. Am. Chem. Soc.* **135** 9829–42
[9] Drofenik J, Gaberšček M, Dominko R, Poulsen F W, Mogensen M, Pejovnik S and Jamnik J 2003 Cellulose as a binding material in graphitic anodes for Li ion batteries: a performance and degradation study *Electrochim. Acta* **48** 883–9
[10] Lestriez B, Bahri S, Sandu I, Roué L and Guyomard D 2007 On the binding mechanism of CMC in Si negative electrodes for Li-ion batteries *Electrochem. Commun.* **9** 2801–6
[11] Kovalenko I, Zdyrko B, Magasinski A, Hertzberg B, Milicev Z, Burtovyy R, Luzinov I and Yushin G 2011 A major constituent of brown algae for use in high-capacity Li-ion batteries *Science* **334** 75–79
[12] Komaba S, Ozeki T and Okushi K 2009 Functional interface of polymer modified graphite anode *J. Power Sources* **189** 197–203
[13] Komaba S, Okushi K, Ozeki T, Yui H, Katayama Y, Miura T, Saito T and Groult H 2009 Polyacrylate modifier for graphite anode of lithium-ion batteries *Electrochem. Solid-State Lett.* **12** A107
[14] Maver U, Znidarsic A and Gaberšček M 2011 An attempt to use atomic force microscopy for determination of bond type in lithium battery electrodes *J. Mater. Chem.* **21** 4071
[15] Magasinski A, Zdyrko B, Kovalenko I, Hertzberg B, Burtovyy R, Huebner C F, Fuller T F, Luzinov I and Yushin G 2010 Toward efficient binders for Li-ion battery Si-based anodes: polyacrylic acid *ACS Appl. Mater. Interfaces* **2** 3004–10
[16] Gómez-Cámer J L, Bünzli C, Hantel M M, Poux T and Novák P 2016 On the correlation between electrode expansion and cycling stability of graphite/Si electrodes for Li-ion batteries *Carbon* **105** 42–51
[17] Jaiser S, Müller M, Baunach M, Bauer W, Scharfer P and Schabel W 2016 Investigations of film solidification and binder migration during drying of Li-ion battery anodes *J. Power Sources* **318** 210–9
[18] Jeschull F, Brandell D, Wohlfahrt-Mehrens M and Memm M 2017 Water-soluble binders for lithium-ion battery graphite electrodes: slurry rheology, coating adhesion, and electrochemical performance *Energy Technol.* **5** 2108–18
[19] Jeschull F, Maibach J, Félix R, Wohlfahrt-Mehrens M, Edström K, Memm M and Brandell D 2018 The solid electrolyte interphase (SEI) of water-processed graphite electrodes examined in a 65 MAh full cell configuration *ACS Appl. Energy Mater.* **1** 5176–88
[20] El Ouatani L, Dedryvère R, Ledeuil J-B, Siret C, Biensan P, Desbrières J and Gonbeau D 2009 Surface film formation on a carbonaceous electrode: influence of the binder chemistry *J. Power Sources* **189** 72–80
[21] Komaba S, Itabashi T, Watanabe M, Groult H and Kumagai N 2007 Electrochemistry of graphite in Li and Na salt codissolving electrolyte for rechargeable batteries *J. Electrochem. Soc.* **154** A322
[22] Gaberšček M, Bele M, Drofenik J, Dominko R and Pejovnik S 2000 Improved carbon anode for lithium batteries—pretreatment of carbon particles in a polyelectrolyte solution *Electrochem. Solid-State Lett.* **3** 171–3
[23] Jeschull F, Brandell D, Edström K and Lacey M J 2015 A stable graphite negative electrode for the lithium–sulfur battery *Chem. Commun.* **51** 17100–3
[24] Lacey M J, Jeschull F, Edström K and Brandell D 2014 Functional water-soluble binders for improved capacity and stability of lithium–sulfur batteries *J. Power Sources* **264** 8–14

[25] Komaba S, Yabuuchi N, Ozeki T, Okushi K, Yui H, Konno K, Katayama Y and Miura T 2010 Functional binders for reversible lithium intercalation into graphite in propylene carbonate and ionic liquid media *J. Power Sources* **195** 6069–74

[26] Mazouzi D, Lestriez B, Roué L and Guyomard D 2009 Silicon composite electrode with high capacity and long cycle life *Electrochem. Solid-State Lett.* **12** A215–8

[27] Mazouzi D, Grissa R, Paris M, Karkar Z, Huet L, Guyomard D, Roué L, Devic T and Lestriez B 2019 CMC-citric acid Cu(II) cross-linked binder approach to improve the electrochemical performance of Si-based electrodes *Electrochim. Acta* **304** 495–504

[28] Delpuech N *et al* 2014 Critical role of silicon nanoparticles surface on lithium cell electrochemical performance analyzed by FTIR, Raman, EELS, XPS, NMR, and BDS spectroscopies *J. Phys. Chem.* C **118** 17318–31

[29] Tranchot A, Idrissi H, Thivel P X and Roué L 2016 Impact of the slurry pH on the expansion/contraction behavior of silicon/carbon/carboxymethylcellulose electrodes for Li-ion batteries *J. Electrochem. Soc.* **163** A1020–6

[30] Kuenzel M, Bresser D, Diemant T, Carvalho D V, Kim G T, Behm R J and Passerini S 2018 Complementary strategies toward the aqueous processing of high-voltage LiNi$_{0.5}$Mn$_{1.5}$O$_4$ lithium-ion cathodes *ChemSusChem* **11** 562–73

[31] Jeschull F, Scott F and Trabesinger S 2019 Interactions of silicon nanoparticles with carboxymethyl cellulose and carboxylic acids in negative electrodes of lithium-ion batteries *J. Power Sources* **431** 63–74

[32] Beaussart A, Petrone L, Mierczynska-Vasilev A, McQuillan A J and Beattie D A 2012 *In Situ* ATR FTIR study of dextrin adsorption on anatase TiO$_2$ *Langmuir* **28** 4233–40

[33] Bridel J S, Azaïs T, Morcrette M, Tarascon J-M and Larcher D 2010 key parameters governing the reversibility of Si/carbon/CMC electrodes for Li-ion batteries† *Chem. Mater.* **22** 1229–41

[34] Schmidt S W, Christ T, Glockner C, Beyer M K and Clausen-Schaumann H 2010 Simple coupling chemistry linking carboxyl-containing organic molecules to silicon oxide surfaces under acidic conditions *Langmuir* **26** 15333–8

[35] Chandrasiri K W D K, Nguyen C C, Parimalam B S, Jurng S and Lucht B L 2018 Citric acid based pre-SEI for improvement of silicon electrodes in lithium ion batteries *J. Electrochem. Soc.* **165** A1991–6

[36] Karkar Z, Guyomard D, Roué L and Lestriez B 2017 A comparative study of polyacrylic acid (PAA) and carboxymethyl cellulose (CMC) binders for Si-based electrodes *Electrochim. Acta* **258** 453–66

[37] Philippe B, Hahlin M, Edström K, Gustafsson T, Siegbahn H and Rensmo H 2016 Photoelectron spectroscopy for lithium battery interface studies *J. Electrochem. Soc.* **163** A178–91

[38] Xu C, Lindgren F, Philippe B, Gorgoi M, Björefors F, Edström K and Gustafsson T 2015 Improved performance of the silicon anode for Li-ion batteries: understanding the surface modification mechanism of fluoroethylene carbonate as an effective electrolyte additive *Chem. Mater.* **27** 2591–9

[39] Hai-Jung P 2016 Unravelling the cell ageing phenomona in aprotic lithium-nickel-cobalt-manganese-oxide batteries *Doctoral Thesis* ETH Zürich (https://doi.org/10.3929/ethz-a-010793448)

[40] Kuenzel M, Bresser D, Kim G T, Axmann P, Wohlfahrt-Mehrens M and Passerini S 2020 Unveiling and amplifying the benefits of carbon-coated aluminum current collectors for sustainable LiNi$_{0.5}$Mn$_{1.5}$O$_4$ cathodes *ACS Appl. Energy Mater.* **3** 218–30

[41] Naumkin A V, Kraut-Vass A, Gaarenstroom S W and Powell C J NIST x-ray photoelectron spectroscopy database (https://doi.org/10.18434/T4T88K)

[42] Kazzazi A, Bresser D, Birrozzi A, Zamory J V, Hekmatfar M and Passerini S 2018 Comparative analysis of aqueous binders for high-energy Li-rich NMC as lithium-ion cathode and the impact of adding phosphoric acid *ACS Appl. Mater. Interfaces* **10** 17214–22

[43] Hochgatterer N S, Schweiger M R, Koller S, Raimann P R, Wöhrle T, Wurm C and Winter M 2008 Silicon/graphite composite electrodes for high-capacity anodes: influence of binder chemistry on cycling stability *Electrochem. Solid-State Lett.* **11** A76

[44] Cuba-Chiem L T, Huynh L, Ralston J and Beattie D A 2008 *In situ* particle film ATR FTIR spectroscopy of carboxymethyl cellulose adsorption on talc: binding mechanism, PH effects, and adsorption kinetics *Langmuir* **24** 8036–44

[45] Klein A, Mayer T, Thissen A and Jaegermann W 2012 Photoelectron spectroscopy in materials science and physical chemistry: analysis of composition, chemical bonding, and electronic structure of surfaces and interfaces *Methods in Physical Chemistry* vol 10 (Weinheim: Wiley-VCH Verlag GmbH & Co. KGaA) pp 477–512

[46] Nordh T, Younesi R, Brandell D and Edström K 2015 Depth profiling the solid electrolyte interphase on lithium titanate (Li$_4$Ti$_5$O$_{12}$) using synchrotron-based photoelectron spectroscopy *J. Power Sources* **294** 173–9

[47] Maibach J, Jeschull F, Brandell D, Edström K and Valvo M 2017 Surface layer evolution on graphite during electrochemical sodium-tetraglyme co-intercalation *ACS Appl. Mater. Interfaces* **9** 12373–81

[48] Jeschull F, Zhang L, Kondracki Ł, Scott F and Trabesinger S 2023 Interphase formation with carboxylic acids as slurry additives for Si electrodes in Li-ion batteries. Part 1: performance and gas evolution *J. Phys. Energy* (https://doi.org/10.1088/2515-7655/acbbed)

[49] Hays K A, Key B, Li J, Wood D L and Veith G M 2018 Si oxidation and H$_2$ gassing during aqueous slurry preparation for Li-ion battery anodes *J. Phys. Chem.* C **122** 9746–54

[50] Rodrigues M T F, Trask S E, Shkrob I A and Abraham D P 2018 Quantifying gas generation from slurries used in fabrication of Si-containing electrodes for lithium-ion cells *J. Power Sources* **395** 289–94

[51] Touidjine A, Morcrette M, Courty M, Davoisne C, Lejeune M, Mariage N, Porcher W and Larcher D 2015 Partially oxidized silicon particles for stable aqueous slurries and practical large-scale making of Si-based electrodes *J. Electrochem. Soc.* **162** A1466–75

[52] Malmgren S, Ciosek K, Hahlin M, Gustafsson T, Gorgoi M, Rensmo H and Edström K 2013 Comparing anode and cathode electrode/electrolyte interface composition and morphology using soft and hard x-ray photoelectron spectroscopy *Electrochim. Acta* **97** 23–32

[53] Ciosek Högström K, Malmgren S, Hahlin M, Gorgoi M, Nyholm L, Rensmo H and Edström K 2014 The buried carbon/solid electrolyte interphase in Li-ion batteries studied by hard x-ray photoelectron spectroscopy *Electrochim. Acta* **138** 430–6

[54] Surace Y, Leanza D, Mirolo M, Kondracki Ł, Vaz C A F, El Kazzi M, Novák P and Trabesinger S 2022 Evidence for stepwise formation of solid electrolyte interphase in a Li-ion battery *Energy Storage Mater.* **44** 156–67

[55] Michan A L, Parimalam B S, Leskes M, Kerber R N, Yoon T, Grey C P and Lucht B L 2016 Fluoroethylene carbonate and vinylene carbonate reduction: understanding lithium-ion battery electrolyte additives and solid electrolyte interphase formation *Chem. Mater.* **28** 8149–59

[56] Gehrlein L, Njel C, Jeschull F and Maibach J 2022 From additive to cosolvent: how fluoroethylene carbonate concentrations influence solid–electrolyte interphase properties and electrochemical performance of Si/Gr anodes *ACS Appl. Energy Mater.* **5** 10710–20

[57] Maibach J, Lindgren F, Eriksson H, Edström K and Hahlin M 2016 Electric potential gradient at the buried interface between lithium-ion battery electrodes and the SEI observed using photoelectron spectroscopy *J. Phys. Chem. Lett.* **7** 1775–80

[58] Lindgren F, Rehnlund D, Pan R, Pettersson J, Younesi R, Xu C, Gustafsson T, Edström K and Nyholm L 2019 On the capacity losses seen for optimized nano-Si composite electrodes in Li-metal half-cells *Adv. Energy Mater.* **9** 1901608

[59] Trill J H, Tao C, Winter M, Passerini S and Eckert H 2011 NMR investigations on the lithiation and delithiation of nanosilicon-based anodes for Li-ion batteries *J. Solid State Electrochem.* **15** 349–56

[60] McDowell M T, Lee S W, Harris J T, Korgel B A, Wang C, Nix W D and Cui Y 2013 *In situ* tem of two-phase lithiation of amorphous silicon nanospheres *Nano Lett.* **13** 758–64

[61] Radvanyi E, Porcher W, De Vito E, Montani A, Franger S and Jouanneau Si Larbi S 2014 Failure mechanisms of nano-silicon anodes upon cycling: an electrode porosity evolution model *Phys. Chem. Chem. Phys.* **16** 17142–53

[62] Campion C L, Li W and Lucht B L 2005 Thermal decomposition of $LiPF_6$-based electrolytes for lithium-ion batteries *J. Electrochem. Soc.* **152** A2327–34

[63] Henschel J, Schwarz J L, Glorius F, Winter M and Nowak S 2019 Further insights into structural diversity of phosphorus-based decomposition products in lithium ion battery electrolytes via liquid chromatographic techniques hyphenated to ion trap-time-of-flight mass spectrometry *Anal. Chem.* **91** 3980–8

[64] Solchenbach S, Metzger M, Egawa M, Beyer H and Gasteiger H A 2018 Quantification of PF_5 and POF_3 from side reactions of $LiPF_6$ in Li-ion batteries *J. Electrochem. Soc.* **165** A3022–8

[65] Jung R, Metzger M, Haering D, Solchenbach S, Marino C, Tsiouvaras N, Stinner C and Gasteiger H A 2016 Consumption of fluoroethylene carbonate (FEC) on Si-C composite electrodes for Li-ion batteries *J. Electrochem. Soc.* **163** A1705–16

[66] Nguyen C C, Yoon T, Seo D M, Guduru P R and Lucht B L 2016 Systematic investigation of binders for silicon anodes: interactions of binder with silicon particles and electrolytes and effects of binders on solid electrolyte interphase formation *ACS Appl. Mater. Interfaces* **8** 12211–20